Blast mitigation strategies for vehicles using shape optimization methods

MASSACHUSETTS INSTITUTE OF TECHNOLOGY
SEP 0 5 2008
LIBRARIES

by

Ganesh Gurumurthy

B.Tech., Mechanical Engineering
Indian Institute of Technology, Madras (2006)

Submitted to the School of Engineering
in partial fulfillment of the requirements for the degree of

Master of Science in Computation for Design and Optimization

at the

MASSACHUSETTS INSTITUTE OF TECHNOLOGY

September 2008

Author .....
School of Engineering
07/08/2008

Certified by .....
Raúl A. Radovitzky
Associate Professor, Aeronautics and Astronautics
Thesis Supervisor

Accepted by .....
Jaime Peraire
Professor of Aeronautics and Astronautics
Co-Director, Computation for Design and Optimization Program

Blast mitigation strategies for vehicles using shape optimization methods

by

Ganesh Gurumurthy

Submitted to the School of Engineering
on 07/08/2008, in partial fulfillment of the
requirements for the degree of
Master of Science in Computation for Design and Optimization

Abstract

This thesis is concerned with the study of blast effects on vehicular structures. The specific problem of a point source blast originating under the vehicle hull is considered, and its impact on the solid body is measured in terms of the total impulse acting on the vehicle. Simplified two-dimensional and three-dimensional computational models are developed to simulate this problem, and the effect of vehicle hull shape on the net impulse loading on the vehicle is analyzed over varying initial blast intensities. Blast mitigation strategies are proposed to minimize blast impact by identifying optimal shapes for the vehicle hull for which net impulse acting on the vehicle is minimized.

Thesis Supervisor: Raúl A. Radovitzky
Title: Associate Professor, Aeronautics and Astronautics

Acknowledgments

Firstly, I would like to thank my advisor, Prof. Raul Radovitzky, for giving me this wonderful opportunity to study and engage in research at MIT. This work would not have been possible without his patience and guidance, and I will be ever grateful for all his support and advice. I would also like to thank the CDO co-directors Prof. Jaime Peraire and Prof. Robert Freund for giving me the chance to be a part of this wonderful program.

Many thanks are due to senior graduate students and post docs in the lab viz. Tan, Ludovic, Antoine and Nayden for helping me out with the codes whenever there was a need, and in giving insightful advice in many situations otherwise. It has truly been inspiring to work with them. It has also been a pleasure getting to know and work with my other labmates Andy, Michelle, Ram, Sudhir, Lei, Mike and Rupa.

I would also like to thank my graduate program administrator Ms. Laura Koller for taking care of all the administrative work for academics and research, and Mr. Brian O'Conaill and Mr. Ed Gazarian for organizing our wonderful lab lunches.

All this would not have been possible but for the sacrifices, encouragement from my parents, my sister and the rest of my family back in India. Last but not the least, I would like to thank my friends at MIT - Anuja, Arvind, Murali, Krupa, Karthik, Harish, Sowmya, members of MCC and numerous others, which I can't quite quote for the list is too long, for making my stay at MIT fun and memorable.

Contents

List of Figures

List of Tables

Chapter 1

Introduction

This thesis is concerned with the development and analysis of models relating to blast effects on vehicles. This chapter describes the relevance of this research to society, summarizes some of the previous work in our area of focus, and outlines the scientific contributions of the thesis.

1.1 MRAPs

As much as 63% of US deaths in the recent wars in Iraq and Afghanistan are known to have been caused by Improvised explosive devices(IEDs) [5]. There has been an urgent need to develop armored military vehicles which are capable of providing protection against such IED attacks and other ambushes in combat zones. This has led to formation of the **Mine resistant ambush protected(MRAP)** vehicles program, and acquisition of these MRAPs has been amongst the Department of Defense's highest priorities in recent times [6].

Shown in Fig:1-2 is an US Marine Corps RG-31 Cougar that rests on its front axle after an improvised explosive device detonated under the vehicle near Camp Taqaddum, Iraq. The IED detonated directly under the vehicle, and its impact, as can be seen from the figure, rendered the vehicle immobile.

Figure 1-1: Example of a vehicle with a clearly visible V-shaped hull

Figure 1-2: BAE's RG-31 damaged by an IED attack obtained from [7]

1.1.1 Design

When a flat-bottomed vehicle, such as a Humvee, hits a mine, a large amount of gas is released which gets trapped underneath the vehicle. As the super heated air from the explosion rapidly expands, it can lift and even throw the 6-ton, up-armored Humvee dozens of feet. Even if the armored crew compartment remains intact, the soldiers inside can be killed by the instant acceleration, which compresses spines and snaps necks.

MRAPs are usually designed with a V-shaped hull to deflect away explosive forces arising from below such that impact on the vehicle itself is minimized, thereby protecting the passenger compartment and the vehicle body. Although these explosive forces usually arise from mine blasts, they could come from IEDs as well. The V-shaped hull design dates back to the 1970s when it was first implemented by a South African Company, Land Systems OMC, in the Casspir armored personnel carrier. Since then several derivatives of this model have been implemented by various military forces around the world. V-hulls are incorporated in armored vehicle designs in several different ways. Following is a brief description of some of the most popular MRAPs and the kind of V-shaped hull design that they possess.

International Maxxpro

International Maxxpro, manufactured by Navistar International accounts for 45% of MRAPs ordered in the year 2007. It uses a body-on-frame chassis, with an armored V-hull crew compartment, and an additional V or semicircular shaped piece protecting the driveline. In such constructions, the body is separate from a rigid frame that supports the drive train of the vehicle. This construction method offers the flexibility to change the design of the vehicle such as the hull without affecting the chassis of the vehicle.

Figure 1-3: Navistar's Maxxpro obtained from [1]

Cougar H

Cougar H, another MRAP which has been in high demand from the US Marines, is manufactured by Force Protection Industries. It has a V-hull crew compartment, and allows the drive line and suspension components to be sacrificed in an attack, while maintaining the safety of the crew. The Cougars have been hit more than 300 times by IEDs and there have been no fatalities so far as of August, 2007 [8].

The deployment of MRAP vehicles has not been without criticisms. Some of the common causes for concerns have been high cost, fuel consumption and varied designs. Also their effectiveness against explosively formed penetrators(EFPs) is still unclear. This alleged threat is being addressed by the next generation MRAP II. One of the models pro-

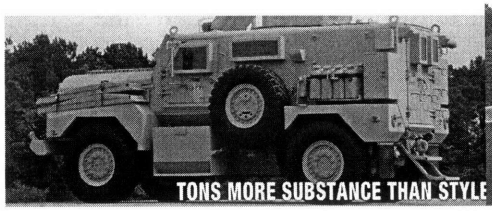

Figure 1-4: Force protection's Cougar-H from [2]

Figure 1-5: Ceradyune Bull from the MRAP II program from [3]

duced under this program is the Ceradyne bull shown in Figure 1-5 which claims to be able to defeat EFP type IEDs [3]. Again this model uses a V-shaped hull.

1.2 Objective

From all the above observations, it's clear that there is an increasing need for better designed vehicles, capable of handling more powerful IEDs, EFPs and other kinds of explosives. In all these instances the hull shape plays an important role in blast mitigation, offering protection by minimizing the damage impact to both the crew and the vehicle. We will focus our attention in this study on the hull shape design more than concerning ourselves with the material itself, and try to develop a better understanding of how the hull shape affects the impact of a blast on the vehicle.

In particular we will develop simple models to simulate blast wave flow around rigid solid objects representative of the vehicle body. As an impact criterion, we choose to calculate the net impulse acting on the solid owing to the blast, and show how the hull shape can be designed so as to minimize blast impact.

1.3 Past work and literature survey

Quite a few studies have been done in the past to analyze the response of vehicle floor plates subjected to blast loading. In [9], the work explored the effect of geometry on floor plates subjected to buried blast loading. In this study, experiments were conducted for varied depths of burial in soil, Stand-off distance(SOD) and plate geometries and their effects on impulse transferred to the target were studied. Results from this research study show that changing the target geometry caused up to a 45% reduction in impulse and this was shown to correlate well with previous experimental results from Gupta [10]. One limitation in these studies was that they were conducted for explosions of very mild intensity and restricted to dihedral shapes . It remains to be seen how the floor plates would respond under strong explosions and other kind of floor plate shapes.

Tremblay [11] derived equations to estimate the total impulse on a blast deflector at an arbitrary orientation from a buried mine blast explosion.This study is based on the empirical equations developed by Westin [12] for specific impulse transmitted to floor plates. Results from this study show a variation in total impulse with change of dihedral angle in V-shaped blast deflectors. Fairlie [13] did a 2D and 3D numerical study of mine blast loading on a circular plate using AUTODYN and also compared results with experimental measurements by calculating momentum transferred to an horizontal pendulum from a mine blast event. Fiserova [14] also did a numerical analysis of mine-blast loading using AUTODYN, focusing more on the effect of soil properties on the impact loading.

From these studies, we can see that there has been a strong interest in buried blast modeling and its impact on a vehicle. However, the focus of most of the studies has been on modeling and analysis of the explosive detonation products that consist of both soil and the blast waves. The effect of blast deflector shape has not been given due importance in these analyses. Even in cases where effects of vehicle floor plate shapes have been considered, the blast intensities and range of shapes considered are extremely limited.

Our contribution will essentially be towards the numerical analysis of vehicle loading under purely blast loading conditons, considering a wider span of generic shapes for the vehicle hull. Analysis of soil effects on the loading of the structure is outside the scope of

this work.

1.4 Structure

In the following chapter we will describe some of the commonly used blast models, and also the model used in our study. Following this, Chapter 3 will provide details on the computational models that are relevant to our study. It will also further elucidate on the fluid and solid solvers used, and describe how the fluid-structure interaction effects have been implemented in our code. Chapter 4 will provide details on the various analyses conducted to explore the effect of shapes, and follow it up with a discussion of the results. Chapter 5 gives the conclusions from this study and suggests the future direction of work from where our understanding stands currently.

Chapter 2

Blast theory and modeling

2.1 Generalities of explosions

During the ignition of an explosive, hot gases at very high pressures are generated. The sudden release of high energy leads to the formation of shock waves. Modeling of the shock waves arising by this sudden energy release from a concentrated source can be done in several ways. Two commonly used initial conditions considered by Brode [15] in the study of spherical blast waves are described below:

2.1.1 Isothermal model

One of the typical methods used is to model the initial conditions of the explosion as an isothermal sphere with pressure p_i and density ρ_i. The sphere is assumed to be uniformly distributed with a certain explosive, for example TNT. The expanding gas from the explosion can be assumed to have a specific heat γ=1.4 at all stages of the process [16].

Given the energy released during the blast E_i, initial temperature T_i, and the initial radius of the sphere r_i, we can determine the initial pressure and density in the sphere as per Equation 2.1:

$$
\begin{aligned}
p_i &= \frac{3(\gamma-1)E_i}{4\pi r^3} + p_a \\
\rho_i &= \frac{p_i}{RT_i}
\end{aligned} \tag{2.1}
$$

where R = 287 $\frac{Pam^3}{kgK}$, the gas constant, and p_a is the atmospheric pressure. For example, let us consider the case of explosion of 1 kg of TNT modeled by a $0.1m$-radius sphere of hot gas with an initial temperature ($T_i = 5T_a = 1465K$). Then one has:

$$
\begin{aligned}
E_i &= 4520\ 10^3 J \\
p_i &= 4295\ 10^5 Pa \\
\rho_i &= 1021.5 kg/m^3
\end{aligned} \tag{2.2}
$$

Extensive numerical simulations have been carried out to establish the time evolution of these blast waves, and empirical formulae giving the variation of blast overpressurewith distance r have been derived in [15] as given by Equation:2.3.

$$
\begin{aligned}
\Delta p_s = & \quad p_a \left[\frac{C_1 E_i}{p_a r^3} + 1 \right] & \text{if } \Delta p_s > 10 p_a \\
\Delta p_s = & \quad p_a \left[\frac{C_2 E_i}{p_a r^3} + \frac{C_3 E_i^{\frac{2}{3}}}{p_a^{\frac{2}{3}} r^2} + \frac{C_4 E_i^{\frac{1}{3}}}{p_a^{\frac{1}{3}} r} - 0.019 \right] & \text{if } 0.1 p_a < \Delta p_s < 10 p_a
\end{aligned} \tag{2.3}
$$

with $C_1 = 0.1567 \frac{m^3 Pa}{J}$, $C_2 = 0.137 \frac{m^3 Pa}{J}$, $C_3 = 0.119 \frac{m^2 Pa^{\frac{2}{3}}}{J^{\frac{2}{3}}}$ and $C_4 = 0.269 \frac{mPa^{\frac{1}{3}}}{J^{\frac{1}{3}}}$.

By knowing the value of the blast overpressure Δp_s at the shock wave front, and using the Rankine-Hugoniot jump relationships, we can determine the density of the fluid just behind the shock wave front from Equation 2.4.

Let ρ_s and p_s refer to density and the pressure just behind the wave front. Then

$$
\begin{aligned}
\rho_s &= \rho_a \frac{[\gamma+1]p_s + [\gamma-1]p_a}{[\gamma-1]p_s + [\gamma+1]p_a} \\
&= \rho_a \frac{7p_a + 6\Delta p_s}{7p_a + \Delta p_s} \text{ if } \gamma = 1.4
\end{aligned} \tag{2.4}
$$

In the above set of equations, Δp_s represents the incident overpressure, p_a the atmo-

spheric pressure and ρ_a the atmospheric density. Using results from any standard textbook such as [17], the fluid behind the shock can be derived as

$$u_s \simeq c_a \frac{5\Delta p_s}{\sqrt{7p_a}} \frac{1}{\sqrt{6\Delta p_s + 7p_a}} \tag{2.5}$$

where c_a is the ambient sound velocity given as $c_a = \sqrt{\frac{\gamma p_a}{\rho_a}}$. When a shock wave is reflected from a target with a zero degree angle of incidence, the reflected overpressure Δp_r is given according to Equation 2.6 as

$$\begin{aligned} \Delta p_r &= 2\Delta p_s + [\gamma + 1]\, q_s \\ &= 2\Delta p_s + \frac{\gamma + 1}{2} \rho_s u_s^2 \end{aligned} \tag{2.6}$$

where q_s is the dynamic pressure. It follows from Equation 2.4 and Equation 2.5 that

$$\Delta p_r \simeq 2\Delta p_s \frac{7p_a + 4\Delta p_s}{7p_a + \Delta p_s} \in [2\Delta p_s, 8\Delta p_s] \tag{2.7}$$

Given in Table 2.1 are the values of specific energy and mass in equivalent TNT for some commonly used explosives obtained from [18]:

Table 2.1: Specific energy of explosives and their mass in equivalent TNT

Explosive	Specific Energy (e_i [kJ/kg])	Mass in eq. TNT ($\frac{W}{m}[kg^{-1}]$)
Nitroglycerine	6700	1.481
TNT	4520	1.0
Semtex	5660	1.250

2.1.2 Point source solution

For very strong explosions, it may be justified to treat the original, central, high pressure area as a point while modeling the initial conditions of a blast. When a finite energy E_0 is packed within a region whose volume shrinks to zero, the pressure in it will theoretically have to rise to infinity. Of all known phenomena, nuclear explosions come closest to realizing these conditions. Under such strong shock assumptions, the initial pressure of the

shock wave is very high and the atmospheric pressure p_0 can be neglected in comparison. This hypothesis allows the use of "similarity property" of the point source solution which was proposed by Taylor in [16]. "Similarity" here means that the spatial distributions of the flow variables will have the same form during a given time interval, the variables differing only in scale. Taylor postulated that under such circumstances the radius of a spherical shock wave propagated outwards in time is

$$R = S(\gamma)t^{\frac{2}{5}}E^{\frac{1}{5}}\rho_0^{-\frac{1}{5}} \tag{2.8}$$

where R is the distance travelled by the shock wave front at time t. E is the Energy intensity of the explosion, ρ_0 the atmospheric density and S(γ) is a calculated function of γ, the ratio of specific heats of air. The effect of the explosion is to force most of the air within the shock front into a thin shell just inside that front. Behind the shock front, the air is in an adiabatic state in which the entropy decreases radially. The similarity assumptions used in [16] for an expanding blast wave of constant energy are

$$\text{Pressure} \quad p/p_0 = y = R^{-3}f_1 \tag{2.9}$$

$$\text{Density} \quad \rho = \rho_0 = \psi \tag{2.10}$$

$$\text{Radial velocity} \quad u = R^{-\frac{3}{2}}\phi_1 \tag{2.11}$$

where f_1, ψ and ϕ_1 are dependent on $\eta = \frac{r}{R}$ where r is the radial coordinate or distance from the point source. Taylor's work was followed by Von Neumann [19] who derived exact solutions for the point source blast wave with the strong shock assumption. The details of the solution method for this can be found in [20]. Sedov [21] also followed the work of Taylor, and derived the point source solution taking counter pressure into account. This work also offers comparisons between different theories of point source solution which include the self-similar solution from [16], and other non self-similar solutions which were derived by [22],[15], and [23] respectively.

From these solution methods, it is observed that since the point source blows away all the material from the origin of the blast, the density around the origin degenerates to zero

while the temperature tends to infinity. Due to this singularity, numerical solutions for point blast can deviate from the exact soluton in the vicinity of the point source origin, and appropriate measures must be taken to enforce to the correct solution close to the origin.

2.2 Currently used blast model

In our current study, we use the point source solution which is based on the non self-similar solution developed by Okhotsimskii [23], and further improved by Bui [24]. The solver consists of an one-dimensional CFD code which solves Equations 2.12 using a finite-difference schemes taking counter pressure taken into account. The solution method is summarized as follows:

2.2.1 Governing equations

Let s and r be the Lagrangian and Eulerian coordinates, respectively. The equations of motion in Lagrangian form is given as

$$\begin{aligned} \frac{\partial r}{\partial s} &= \frac{s^{j-1}}{r^{j-1}}\frac{\rho_0}{\rho} \\ \frac{\partial u}{\partial t} &= -\frac{1}{\rho}\frac{\partial p}{\partial s}\frac{\partial s}{\partial r} \\ \frac{\partial r}{\partial t} &= u \\ \frac{\partial \mathcal{U}}{\partial t} &= 0 \end{aligned} \tag{2.12}$$

where $\mathcal{U}$ is some function of the entropy p/ρ^{γ} , j=1,2,3 corresponding to the planar, cylindrical and spherical symmetries.The variables s,t,p, u and r are then non-dimensionalized as

$$\begin{aligned} \sigma &= \frac{s}{E^{1/j}p_0^{-1/j}}; \quad \tau = \frac{t}{E^{1/j}\rho_0^{1/2}p_0^{-\frac{2+j}{2j}}}; \quad \bar{p} = \frac{p}{p_0} \\ \bar{\rho} &= \frac{\rho}{\rho_0}; \quad \bar{u} = \frac{u}{\sqrt{p_0/\rho_0}}; \quad \xi = \frac{r}{E^{1/j}p_0^{-1/j}} \end{aligned} \tag{2.13}$$

Where E $=\alpha E_0$ and $\alpha = 1/\alpha_0$ where α_0 = 0.5385, 0.9840 and 0.8510 corresponding to planar, cylindrical and spherical symmetries respectively.

Introducing new variables,

$$\tilde{p} = \bar{p}^{\frac{\gamma-1}{2\gamma}}; \quad \theta = \mathcal{V}^{\frac{1}{2\gamma}},$$

and φ and ψ as

$$\frac{2\sqrt{\gamma}}{\gamma-1}\tilde{p}\theta + u = \theta\varphi, \tag{2.14}$$

$$\frac{2\sqrt{\gamma}}{\gamma-1}\tilde{p}\theta - u = \theta\psi, \tag{2.15}$$

and after performing a set of operations, the equations of motion are rewritten in terms of dependent variables φ, ψ, θ and ξ

$$\begin{aligned}
\frac{\partial\varphi}{\partial\tau} &+ \mu\frac{\partial\varphi}{\partial\sigma} + \lambda + \nu'\frac{\partial\theta}{\partial\sigma} = 0, \\
\frac{\partial\psi}{\partial\tau} &- \mu\frac{\partial\psi}{\partial\sigma} + \lambda + \nu'\frac{\partial\theta}{\partial\sigma} = 0, \\
\frac{\partial\xi}{\partial\sigma} &= \frac{\sigma^{j-1}}{\xi^{j-1}}\frac{\theta^2}{\left[\frac{\gamma-1}{4\sqrt{\gamma}}(\varphi+\psi)\right]^{\frac{2}{\gamma-1}}}, \\
\frac{\partial\theta}{\partial\tau} &= 0
\end{aligned} \tag{2.16}$$

where

$$\begin{aligned}
\lambda &= (j-1)\frac{\gamma-1}{8}\frac{\theta(\varphi^2-\psi^2)}{\xi}, \\
\mu &= \sqrt{\gamma}\left[\frac{\gamma-1}{4\sqrt{\gamma}}\right]^{\frac{\gamma+1}{\gamma-1}}\frac{(\varphi+\psi)^{\frac{\gamma+1}{\gamma-1}}\xi^{j-1}}{\theta\sigma^{j-1}}, \\
\nu' &= \frac{\varphi-\psi}{2\theta}\mu, \quad \nu = \nu'\frac{\partial\theta}{\partial\sigma}
\end{aligned}$$

2.2.2 Solution method

In the first time step, when $\tau = \tau_0$, the blast is assumed to be very close to the origin and the strong shock analytical solution of Sedov or Von Neumann is applied in the interval $[0, \sigma^0]$. This solution is advanced in time and space by integrating the system of equations 2.16 numerically. In order to do that the (τ, σ) plane is divided into a computational net as follows. The τ-axis is first divided into equal subintervals such that $\tau^n = \tau^{n-1} + \Delta\tau$. and then the interval $[0, \sigma^0]$ is divided into k^0 subintervals, i.e. $\sigma_{i+1} = \sigma_i + \Delta\sigma_{i,i+1}, i = 0, \ldots, k^0$. The distance the blast wave front can travel in the time $\Delta\tau$ is given as

$$\Delta\sigma = \Delta\tau c^n, \tag{2.17}$$

where the superscript n denotes the n^{th} time step, and hence the n^{th} row in the computational net. Therefore, one computational point is added on the $(n+1)^{th}$ row so that

$$k^{n+1} = k^n + 1. \tag{2.18}$$

Using the symmetry boundary conditions at the point source origin and the Rankine-Hugoniot conditions at the blast wave front, the non-linear PDEs from Equation 2.16 are discretized and solved explicitly using the Picard iteration in each time step and advanced forward in time. At the end of each time step the flow variables can be obtained from the dependent variables as follows

$$u_i^{n+1} = \left[\frac{\gamma - 1}{4\sqrt{\gamma}}(\varphi_i^{n+1} + \psi_i^{n+1})\right]^{\frac{2\gamma}{\gamma-1}}, \tag{2.19}$$

$$p_i^{n+1} = \frac{1}{2}\theta_i^{n+1}(\varphi_i^{n+1} - \psi_i^{n+1}), \tag{2.20}$$

$$\rho_i^{n+1} = \frac{(p_i^{n+1})^{1/\gamma}}{(\theta_i^{n+1})^2} \tag{2.21}$$

Using this model, we can solve for the blast wave solution of planar, cylindrical and spherical blasts up to any desired distance. This is particularly useful since solving the one-dimensional CFD code is extremely fast. The solution obtained from this code is given

as an initial condition to shock flow problems solved on higher dimensional domains which require more intensive computations.

The constants that need to be specified as input parameters for blast initialization are E_0, P_0, ρ_0 and γ. Also specified as part of the inputs are the coordinates of the origin of the blast, distance up to which the blast solution needs to be solved, and the type of the blast itself viz. planar, cylindrical or a spherical blast.

2.2.3 Validation

This blast model has been validated by comparing with other experiments and numerical codes involving air blasts with spherical symmetry. The other numerical models and experimental studies used for comparison are described in [25] and [4] and results from the validation study can be found in [26]. A test layout for the measurement of the different metrics is shown in Figure 2-1.

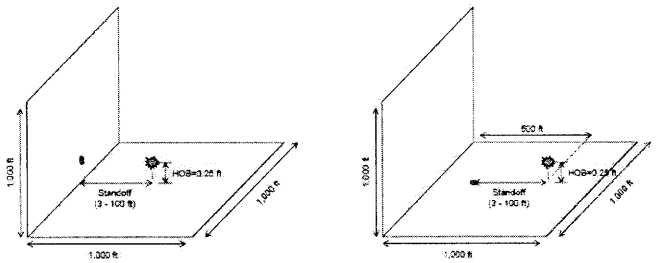

Figure 2-1: Schematic of test layout from [4]

Good agreement was found to exist for important metrics such as the Incident and reflected, pressures and impulse . Shown in Figure 2-2 and 2-3 are comparisons of the incident positive scaled impulse and reflected positive scaled pressure between the current model and previously developed numerical models and experimental results.

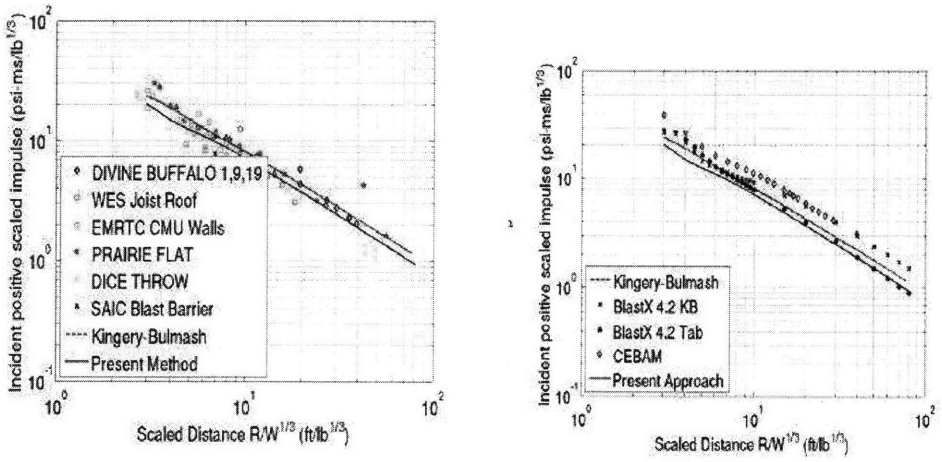

(a) Comparison with experiments

(b) Comparison with other CFD codes

Figure 2-2: Comparison of incident positive scaled impulse with other numerical and experimental models

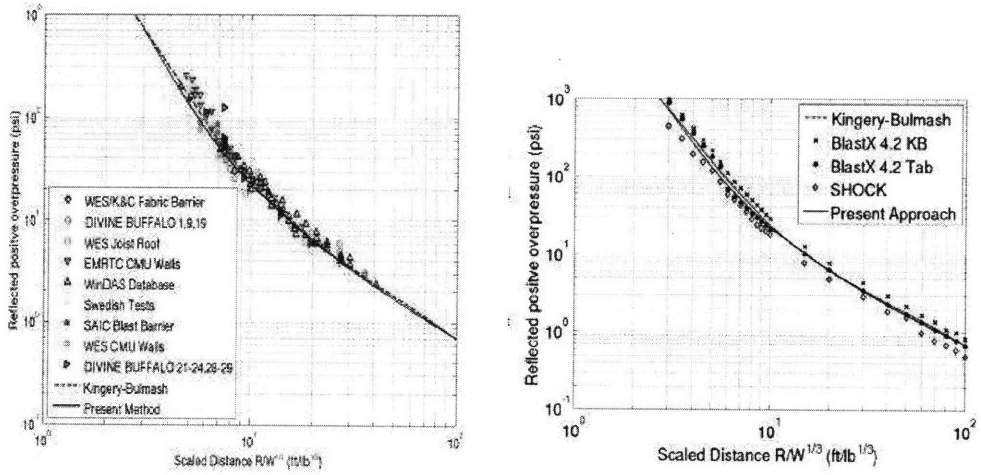

(a) Comparison with experiments

(b) Comparison with other CFD codes

Figure 2-3: Comparison of reflected positive overpressure with different numerical and experimental models

Chapter 3

Computational models

In this chapter we will present the computational models that were used to conduct the various analyses. Two types of analyses were conducted : two-dimensional and three-dimensional studies. Details for each of these models will be presented in the following sections elaborating separately on the representation of the solid and the fluid in each case.

3.1 Two dimensional modeling

As described earlier, we wish to model the flow of a blast wave around a vehicle and measure its impact on the vehicle body over time. Since we are modeling this in 2D, we will consider a cross-section along the mid-section of the vehicle and parallel to the frontal plane. This cross sectional plane also contains the point source of the blast, as shown in the schematic Figure 3-1.

3.1.1 Fluid modeling

The fluid model consists of: blast initialization, blast propagation and reflection at the solid boundary. We use the point source solution developed by Bui [24], and model the explosion under the vehicle as a cylindrical blast. E, ρ, p and γ are specified as constants to the blast initialization code, where E is the blast intensity in J/m, ρ is the density of air, p is atmospheric pressure, and γ the ratio of specific heats of air. Also given as inputs to the

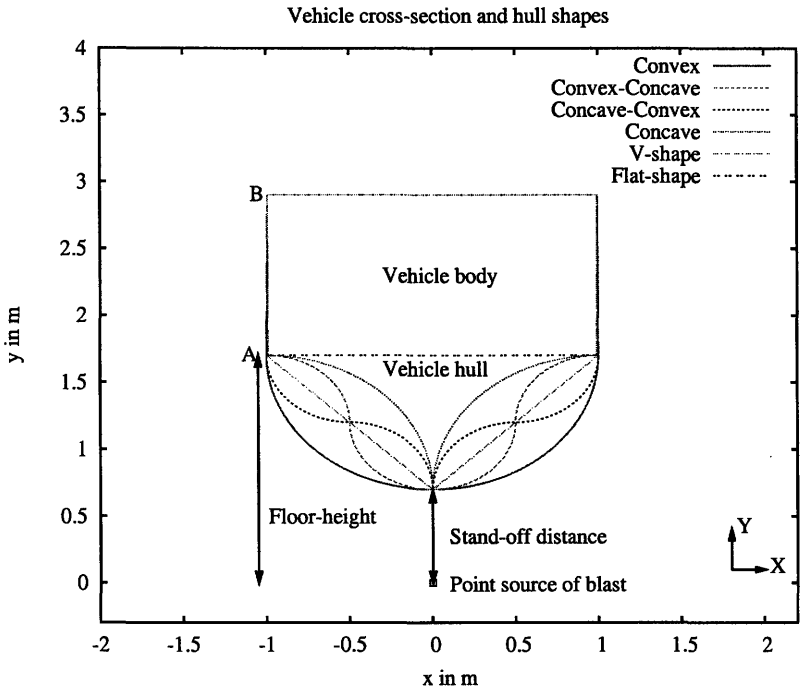

Figure 3-1: Schematic layout of a 2D problem

code are the origin of the blast and the radial distance from the origin up to which the blast needs to be initialized.

Once this initialization is done, the hydrodynamic values from this solution are interpolated over the fluid grid using cubic spline interpolation. The fluid grid is generated by AMROC (Adaptive mesh refinement using object oriented C++) [27], a mesh adaption framework designed for the solution of hyperbolic fluid flow problems on distributed memory machines. In these set of simulations, AMROC uses an external package called Clawpack (Conservation LAWs software PACKage) [28] to solve the euler equations over the fluid domain.

The Clawpack code requires that the user specify a Riemann solver for the problem being solved and a subroutine that implements the boundary conditions. Source terms can also be handled in which case a subroutine must also be supplied to solve the source terms over one time step. In our case, this was done by giving the interpolated values of the blast initialization as described earlier. The equations are solved over logically rectangular grids

and this is adapted to block structured grids with parallelization implemented in AMROC.

3.1.2 Solid representation

In order to model complex boundaries within cartesian meshes, level set methods have recently become very popular. The boundary is represented implicitly with a scalar function ϕ that stores the signed distance to the boundary surface and allows the direct evaluation of the boundary outer normal at every mesh point as $\mathbf{n} = \nabla\phi/|\nabla\phi|$ [29].

The level set method in our simulations uses some of the cells on the Cartesian fluid mesh to enforce immersed boundary conditions [30] between the solid and fluid before a numerical update. This step involves interpolation and/or extrapolation operations to construct appropriate values in those "internal ghost cells" which represent the solid (refer Figure 3-2). A cell is considered to be a valid fluid cell near the boundary if the distance in the cell midpoint is positive and is treated as solid otherwise. Conservation errors and numerical "staircase" artifacts at the boundary are minimized by the use of block-structured dynamic adaptation of the mesh.

The boundary condition at a rigid wall moving with velocity $\mathbf{w}$ is $u \cdot n = w \cdot n$. Enforcing this within ghost cells will require mirroring of the values of ρ, $\mathbf{u}$, p across the embedded boundary and a velocity modification within the ghost cells as per Equation 3.1.

$$\mathbf{u}' = 2((\mathbf{w} - \mathbf{u}) \cdot \mathbf{n})\mathbf{n} + \mathbf{u} \tag{3.1}$$

The mirrored values in a ghost cell center $\mathbf{x}$ are then calculated by spatially interpolated values at the point $\mathbf{x} = \mathbf{x} + 2\phi\mathbf{n}$ from neighboring interior cells. Figure 3-2 shows the interpolation locations indicated by the origin of arrows normal to the complex boundary(dotted).

3.2 Three dimensional modeling

Three dimensional modeling is in many ways similar to that of two dimensional modeling. However there are a few concepts that are different or exclusive to the three-dimensional

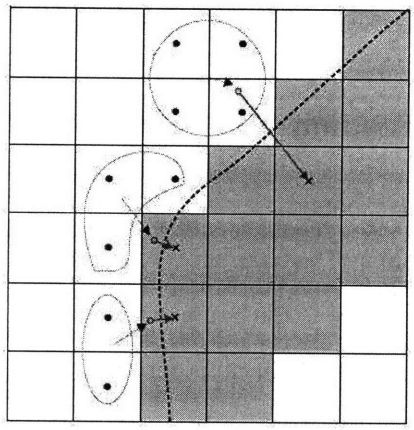

Figure 3-2: Interpolation stencils for the construction of values in interior ghost cells (gray) at an embedded rigid wall obtained from [31]

models which will be discussed in this section.

3.2.1 Fluid modeling

Blast initialization is done using the point source solution developed by Bui [24]. However in this case, the solution is obtained for a spherical blast wave and interpolated using the cubic interpolation on a 3D fluid grid. Riemann solvers for 3D euler equations are used in this case and interfaced with AMROC as described earlier.

3.2.2 Solid representation

The main difference between 2D and 3D modeling is the way the solid has been modeled. Unlike the 2D case, in 3D the solid is considered as a deforming object. Hence the full interaction between the solid and the fluid is accounted for explicitly by the numerical method. In the simulation studies, the solid meshes are created using a finite element modeling software ABAQUS [32] using tetrahedral elements. A separate computational solid dynamics(CSD) solver ADLIB [33] is used to study the response of the solid to the hydrodynamic loading produced by a blast. It uses an advanced parallel finite-element simulation capability based on a Lagrangian large-deformation formulation of the equations of motion [34].

3.2.3 Fluid structure interaction

Fluid structure interaction(FSI) is an important concept utilized by these 3D simulations. This is implemented in the Virtual test facility(VTF) [33] which is a software environment for coupling solvers for compressible CFD(in AMROC) with solvers for CSD(in ADLIB). The CFD solvers facilitate the computation of flows with strong shocks as well as fluid mixing. The CSD solvers provide capabilities for simulation of dynamic response in solids such as large plastic deformations, fracture and fragmentation. In addition, the VTF can be used to simulate highly coupled fluid-structure interaction problems such as high rate deformation of metallic solid targets forced by the detonation of energetic materials, which is similar to scenarios we consider in our simulations.

This technique assumes that the fluid and solid domains are disjoint and that the interaction takes place only at the fluid-solid interface. The information exchange between the fluid and solid solvers is reduced to communicating the velocities and geometries of the solid surface to the Eulerian fluid mesh and imposing the hydrostatic pressure onto the Lagrangian solid as a force on its exterior.

A key issue that arises with this approach is how to represent the evolving surface geometry on the Eulerian fluid mesh. As described earlier for the 2D solid representation, the VTF uses a "ghost fluid" cell approach whereby a diffused boundary technique is used in which some interior cells are used directly to enforce the embedded boundary conditions in the vicinity of the solid surface. One advantage of this approach is that the numerical stencil is not modified, thus ensuring optimal parallel scalability. Also conservation errors and the numerical "staircase" artifacts at the embedded boundary are minimized by the use of a block-structured dynamic adaptation of the mesh in AMROC. As the solid deforms, the solid-fluid boundary is implicitly represented with a scalar level set variable that is updated on-the-fly using the closest-point transformation algorithm (CPT) [35]. The CPT effectively allows the explicit description of a triangulated surface mesh into the signed distance function. It computes for every discrete point on the Cartesian grid the nearest point on the surface mesh. A number of publications provide details about the coupling approach, including numerical properties and validation [31, 36, 37, 38].

Chapter 4

Analysis and discussion

4.1 Study of basic shapes

In this study, some basic shapes for the hull were considered and their influence on the impact of the blast wave on the solid and its flow around the object were studied. A schematic layout of the different shapes considered in these set of simulations is shown in Figure 4-1.

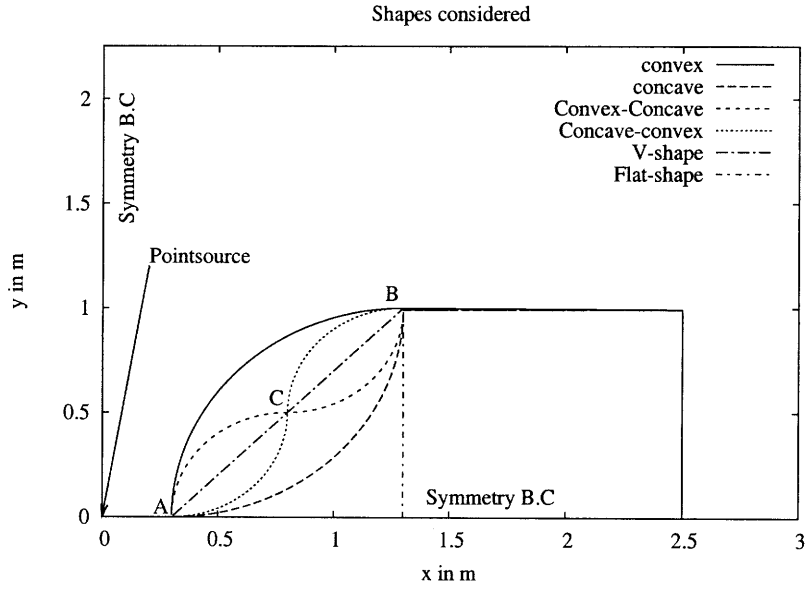

Figure 4-1: Schematic layout of different shapes

- **Concave shape** consisting of a quarter circle, concave upwards, between points A and B
- **Convex shape** consisting of a quarter circle, convex upwards, between points A and B
- **Convex-Concave shape** consisting of two quarter circles, convex upwards between points A and C, and concave upwards between points C and B
- **Concave-Convex shape** consisting of two quarter circles, concave upwards between points A and C, and convex upwards between points C and B
- **V-shape** consisting of a straight line joining points A and B
- **Flat-shape** or no hull, consisting of a vertical straight line through B

4.1.1 Geometry

Each of the curves shown in Figure 4-1 passes through points A and B, thus making the stand-off distance(SOD), measured as the distance from the point source to the front-tip point A, being 0.3 m for every shape except the flat-shape for which it is 1.3 m. The curve from A to B represents the shape of the hull. Behind point B is a rectangular region of the solid object which represents the body of the vehicle. The dimensions of the solid object used in these simulations approximately reflect the actual dimensions of a Cougar-H MRAP vehicle [2]. The ground clearance in this case is the SOD, which is taken to be 30 cm. Half-width of the vehicle is taken to be 1.0 m, and the total height of the vehicle is 2.5 m. The Cougar-H uses a V-shaped hull whose cross section is roughly the same as the one used for this simulation.

4.1.2 Initial conditions

Thus we are essentially considering a simplified 2D cross section of a standard MRAP (taken perpendicular to its length) and comparing its performance with other possible shapes for the hull. The solid object is assumed to be rigid and stationary and thus the

ghost-fluid boundary is kept fixed throughout the entire simulation. Energy release for the cylindrical blast wave from the point source is specified as an input parameter with the units J/m as this a 2D problem. The one dimensional point source CFD code is solved up to a distance of 2 cm lesser than the SOD from the point source, its values are interpolated over the fluid mesh and given as the initial condition to this simulation.

4.1.3 Boundary conditions

In this simulation setup we assume that the point source lies on the line of symmetry for the solid shape. This type of arrangement will be referred to as centerline symmetry. The domain lying on only one side of the line of symmetry is considered for meshing, while applying symmetry boundary conditions along the same. By doing so, the computational effort for the simulation is reduced by half.

Two types of boundary conditions are considered:

- **Surface blast** The point source is chosen to lie on the left boundary, and symmetric boundary conditions are applied to it in order to model a semi-cylindrical surface blast.

- **Air blast**The left boundary is chosen to be to the left of the point source and outflow conditions are applied to it. Such a scenario corresponds to a fully cylindrical air blast wave.

4.1.4 Simulations setup

Figure 4-2 shows the typical mesh layout at the beginning of a simulation. Three levels of refinement including base level are used on a block structured grid with adaptive mesh refinement generated using AMROC [27]. The boundary is represented implicitly with a scalar function ϕ that stores the signed distance to the solid surface. Since AMROC selectively refines the mesh along internal boundary lines, as observed in Figure 4-2, mesh elements are finer around the solid boundary and the blast wavefront. This is useful to obtain a well defined solid geometry and cylindrical shock front in a cartesian mesh, and helps in minimizing error created by the numerical "staircase" artifacts along these boundaries.

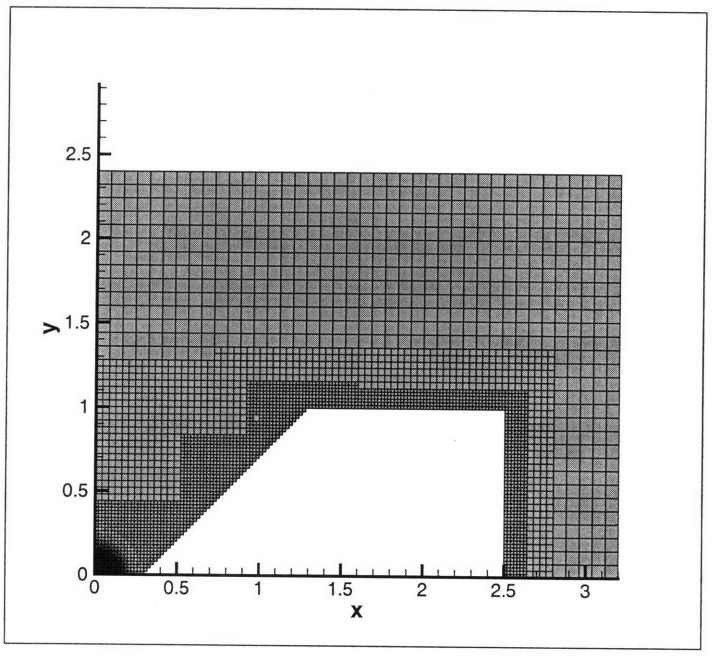

Figure 4-2: Mesh layout for a V-shaped plate ahead of a blast

The simulations are carried out for a total time of 7 ms using 4 processors for each run. The variables recorded during the course of the simulation included the net force acting on the object in the x and y directions at each time step, with the x axis being along the line of symmetry. The forces acting on the body at each time step in the x and y directions are determined by measuring the overpressure on a set of data points lying along the boundary of the solid object, and integrating their value over the entire boundary of the object according to Equation 4.1 and Equation 4.2. By integrating the total force acting on the body over all the time steps,the impulse acting on the body is estimated using in Equation 4.3. The impulse is calculated in the units of Pa.m.secs as the body is two dimensional. It can be split into two components: head-on impulse measured on the hull and the back face using Equation 4.1 and Equation 4.3, and the side-on impulse which is measured as the impulse acting on the top face of the solid object using Equation 4.2 and Equation 4.3. The multiplying factor of 2 is used in Equation 4.1 because we are considering only one half of the hull and the total force on the hull will be twice as much. Maximum values of the head-on impulse and the side-on impulse are used as the most

important criteria to assess the impact of the blast on the solid object.

$$\mathbf{F_x} = \int_{\partial\Omega} \mathbf{2(p - p_0)}\, \hat{\mathbf{e}}_\mathbf{x} \cdot \vec{ds} \tag{4.1}$$

$$\mathbf{F_y} = \int_{\partial\Omega} \mathbf{(p - p_0)}\, \hat{\mathbf{e}}_\mathbf{y} \cdot \vec{ds} \tag{4.2}$$

$$\mathbf{I} = \int \mathbf{F}\, dt \tag{4.3}$$

In the equation above, $\vec{ds}$ refers to the elemental length ds over which the overpressure $(p - p_0)$ acts.

Simulations are carried out for varying levels of the initial blast intensity in order to observe the effect of blast intensity on performance of each shape. The energy levels that are considered are 0.80 MJ/m, 4.0 MJ/m, 20.0 MJ/m and 40.0 MJ/m respectively. It is to be noted that 4.0 MJ corresponds to the energy release from 1 kilogram of TNT.

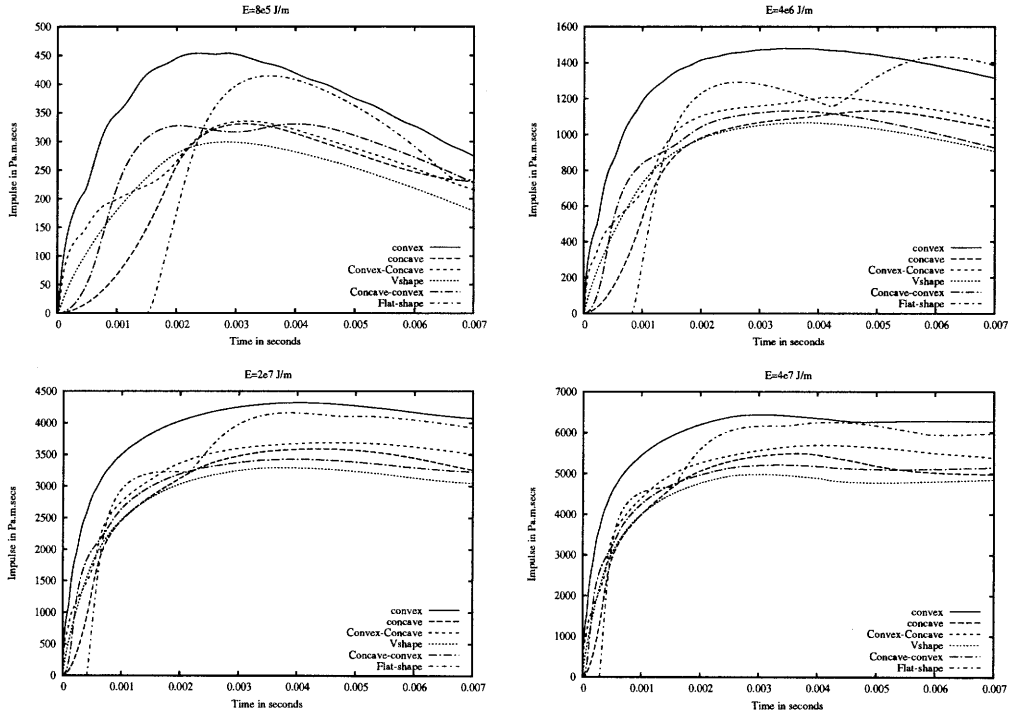

Figure 4-3: Head-on impulse evolution on the bodies for a surface blast. Energy intensity of the blasts considered are $8 \times 10^5 J/m$,$4 \times 10^6 J/m$,$2 \times 10^7 J/m$ and $4 \times 10^7 J/m$ respectively

Surface blast

Shown in Figure 4-3 are the results of the head-on impulse evolution for the different energy levels that are considered. It is observed that in each case, the head-on impulse builds up to a maximum and then tails off to a lower value over time. This is so because initially the blast wave flows over the hull with a high pressure, thereby generating a strong positive force acting on the solid. This leads to a rapid build-up of the head-on impulse on the solid. This rate of impulse build up is related to the peak force load acting on the solid, and this in turn is dependent on the hull shape at its tip. It can be seen that shapes with a narrow and pointed tip such as the concave, concave-convex and to an extent V-shape, have a lower rate of impulse buildup than those which are flatter such as the convex shape. This is so because a blunt front tip presents a low angle of incidence to the incoming blast wave, creating higher reflected pressures and higher net force acting on the solid in the x-direction.

As the blast wave flows around the solid, the pressure acting on the hull reduces, while the pressure on the back face of the solid object increases. This leads to a net negative force acting on the body in the x-direction. Hence the head-on impulse reaches a maximum and then starts decreasing in value. We are interested in studying this value of peak head on impulse acting on the body as our primary criterion in assessing blast impact.

Over all blast intensity levels, we observed that the V-shape showed the best performance in terms of minimizing the peak head-on impulse and the convex shape performed the worst. For the convex shape and flat-shape, it is observed that there are repeated reflections of the blast wave between the solid and the left boundary where symmetry boundary conditions are applied. This led to repeated loading on the solid object as can be seen from the bumps on the impulse evolution curve for the convex shape for energy intensity of 0.8 MJ/m in Figure 4-3. Also, it must be noted that the convex and flat-shapes suffer from the secondary reflected blast waves. In one-dimension point source codes, these secondary reflected waves are caused by the singularity of the explosion center which causes the primary reflected wave to reflect back towards the plate. A similar effect is seen with the convex and flat shaped hulls, which behave approximately as a planar obstacle would

at distances very close to the point source explosion.

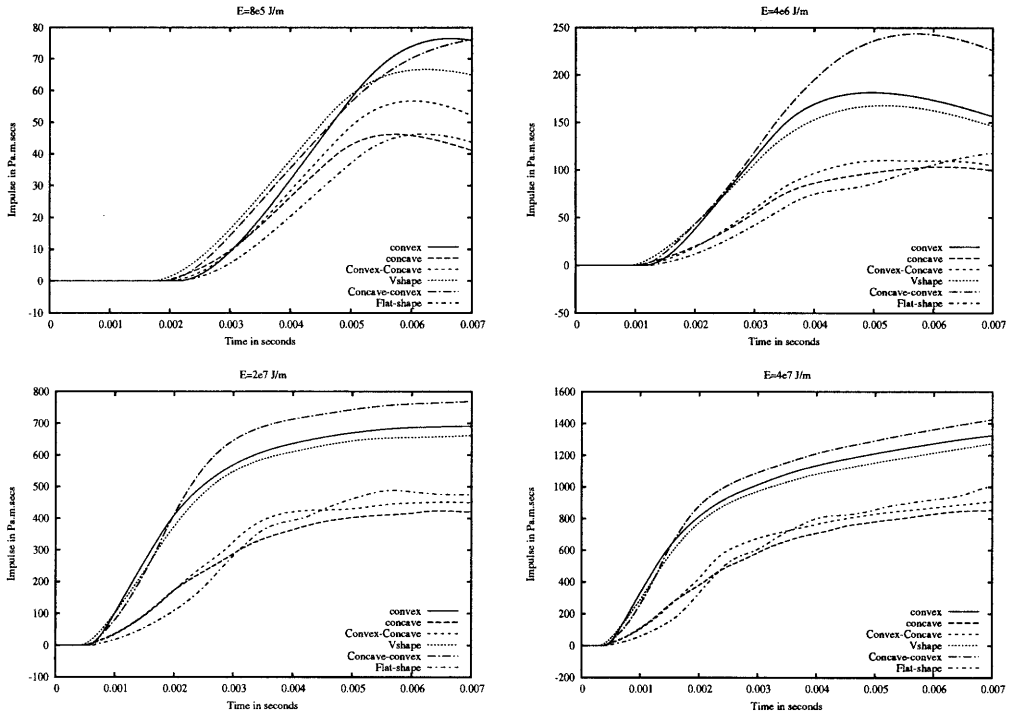

Figure 4-4: Side-on impulse evolution on the bodies for a surface blast. Energy intensity of the blasts considered are $8 \times 10^5 J/m$,$4 \times 10^6 J/m$,$2 \times 10^7 J/m$ and $4 \times 10^7 J/m$ respectively

Yet another reason could be the fact that the convex and flat-shapes suffer from secondary blast reflections, as described earlier.

Shown in Figure 4-4 are the side-on impulse evolution curves for different blast intensities. Side-on impulse ,in this case, is obtained by integrating the net force acting on the top surface of the solid over time using Equation 4.2 and Equation 4.3. From these set of curves, we observe that at all blast intensities, apart from the flat-shape, the concave and convex-concave shapes are the most effective in reducing the side-on impulse. There is a marked difference in the peak impulse values for these shapes when compared with the rest. The concave and convex-concave shapes show as much as 30-40% reduction in maximum impulse over other shapes such as the convex, concave-convex and the V-shape.

It can be seen that the concave shapes have a natural tendency to deflect the incoming blastwave away from the body of the vehicle in a transverse direction. On the other hand,

the convex shapes will make the blastwave flow around them, thereby leading to greater side-on impulse acting on the top-face of the solid object. The schematic shown in Figure 4-5 gives a qualitative explanation for this shape effect on the movement of the blast wave, and hence the side-on impulse values.

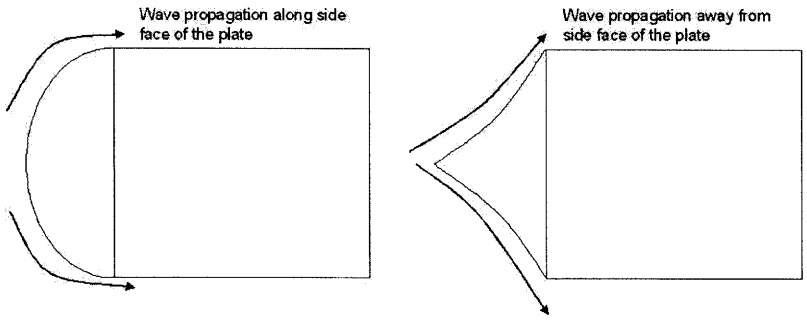

Figure 4-5: An illustrative view showing effect of curve shape on wave propagation direction. Concave shapes deflect the blast wave away from the side face of the vehicle while convex shapes will have opposite response.

It is seen that over all energy levels, the side-on impulse values are lower than the corresponding values for head-on impulse. This is expected because while measuring the head-on impulse, the pressure being measured on the surface and integrated is reflected overpressure which is the static overpressure times the reflection coefficient, whereas in the case of side-on impulse, the pressure being measured on the surface and integrated is the static pressure itself. This is due to the near ninety degree angle of incidence of the blast wave with the top surface which causes the reflection coefficient to be one in this case. Besides, by the time the pressure wave reaches the top surface of the solid where the side-on impulse is measured, there is a significant drop in the peak overpressure of the blast wave. This could also be another reason why we observe lower side-on impulse values.

Free air blast

The same set of simulations are then carried out with a change of boundary conditions. Instead of imposing reflection boundary conditions on the left boundary of the computational domain, we apply outflow conditions on the left boundary. This study models a fully

cylindrical air blast wave and also can be compared with the surface blasts to check for any shape effects.

This boundary condition also models a free explosion in air unlike the earlier case where we modeled a surface blast. The following curves shown in Figure 4-6 and 4-7 present the results for the head-on and side-on impulse evolution for various shapes subjected to blasts of varying intensity.

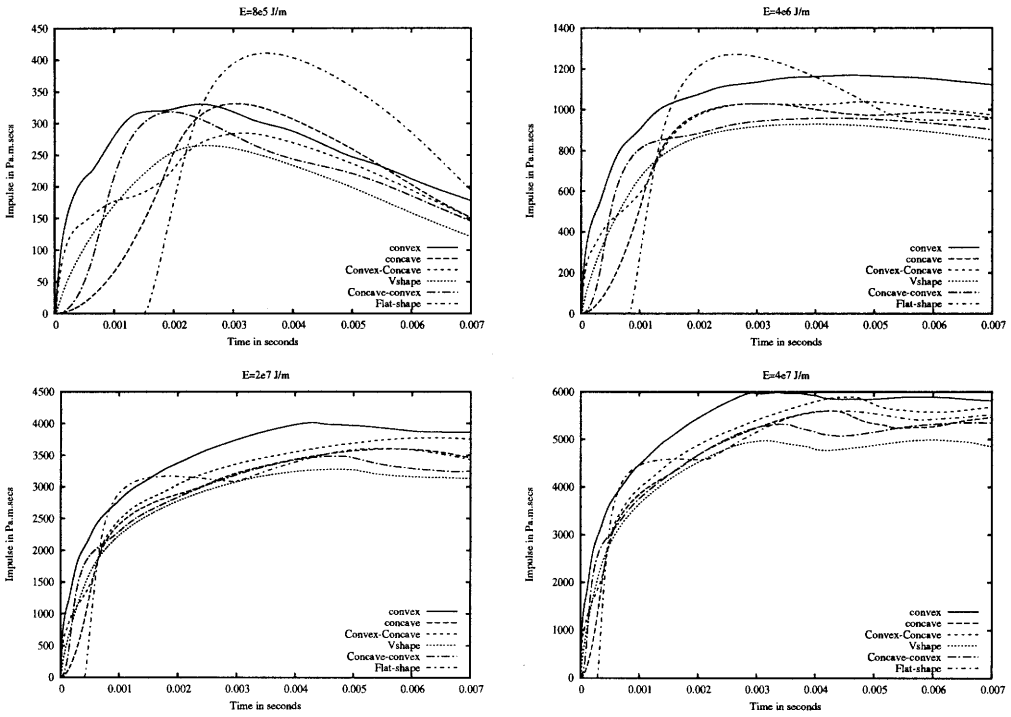

Figure 4-6: Head-on impulse evolution on the bodies for a free air blast. Energy intensity of the blasts considered are $8 \times 10^5 J/m$,$4 \times 10^6 J/m$,$2 \times 10^7 J/m$ and $4 \times 10^7 J/m$ respectively

From Figure 4-6 we see that even under impact from an air blast wave, the V-plate performs the best in terms of minimizing the peak head-on impulse at all energy levels. Similarly we observe from Figure 4-7 that the side-on impulse is minimized when the flat-shape is used, followed by concave and the convex-concave shapes which are second lowest. We observe a significant reduction in the maximum side-on impulse values for these two shapes over the remaining set of shapes as seen before with the surface blast initial conditions. As explained earlier with schematic Figure 4-5, these two shapes will

push the incident blast wave into a lateral direction, so that the impact of the blast wave on the top face is reduced. As observed from the snapshots shown in Figures 4-8 and 4-9 at time instant t = 1 ms, we can see that these two shapes are most efficient in pushing away the blast into a lateral direction as compared to the rest of the shapes at the same time instant. This shows why these shapes cause reduction in the side-on impulse.

It is also interesting to note here that although head-on impulse values are significantly higher than the side-on impulse values for the lowest energy levels (about seven times at E=8e5 J/m), this ratio decreases as the blast intensity is increased. At a blast intensity of 40 MJ/m, we notice that the maximum head-on impulse values is just about three times the maximum side-on impulse values.

This could be due to the fact that at higher blast intensities, the blast wave travels faster, and this limits the time of interaction between the incident and reflected pressure waves. Thus the blast wave would reach the top surface sooner, and also with a higher peak overpressure, causing a relative increase in side-on impulse values over the head-on impulse.

This trend shows that though side-on impulse values may be lower in magnitude at lower energy levels, they become comparable to the head-on impulse at higher blast intensities, and thus should not be discounted while analyzing the design of hull shapes.

4.1.5 Comparison between effects of shape on Air blasts and Surface blasts

Figure 4-13 offers a comparison of the head-on impulse curves for a blast intensity of 4 MJ/m for the given two boundary conditions. Let us, for example, consider the case of flat shape in both these figures. It can be seen that there is an initial rise in the impulse values, followed by a secondary increase. It can be seen that in both the cases, the first peak on both the head-on impulse values are almost equal at around 1280 Pa.m.sec. However, while the second peak in case (a) is over 1400 Pa.m.sec, in case (b) the second peak impulse value is lesser than that of the first peak i.e. 1280 Pa.m.sec . This could imply that the reflection boundary condition applied to the left boundary in the case of surface blasts contributes to

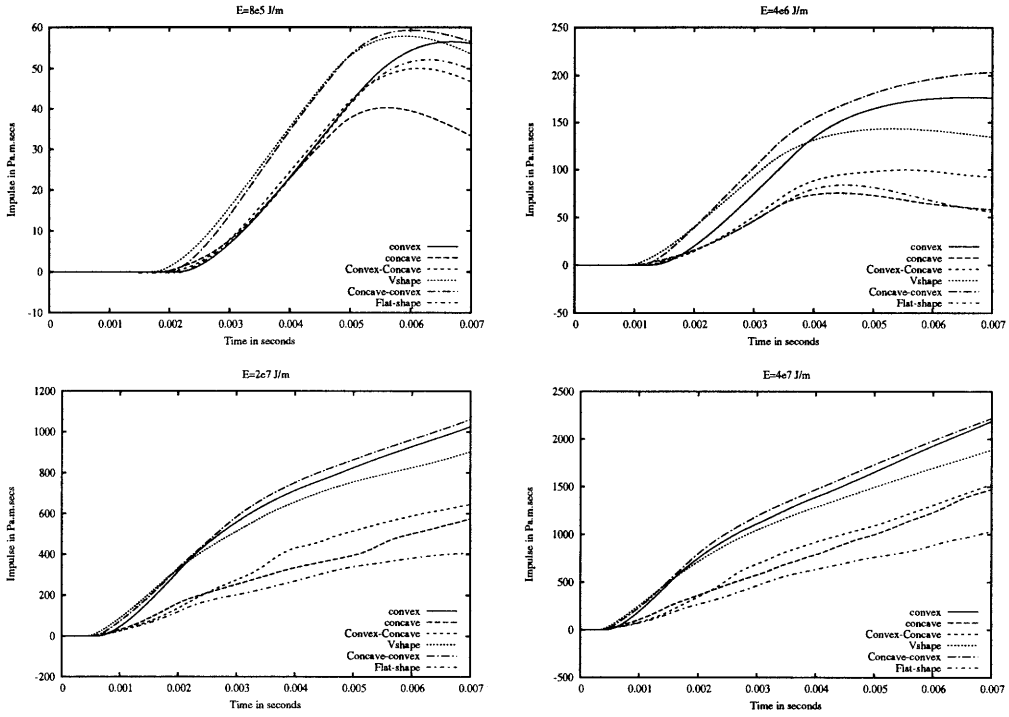

Figure 4-7: Side-on impulse evolution on the bodies for a free air blast. Energy intensity of the blasts considered are $8 \times 10^5 J/m$,$4 \times 10^6 J/m$,$2 \times 10^7 J/m$ and $4 \times 10^7 J/m$ respectively

an enhanced secondary presure wave acting on the hull.

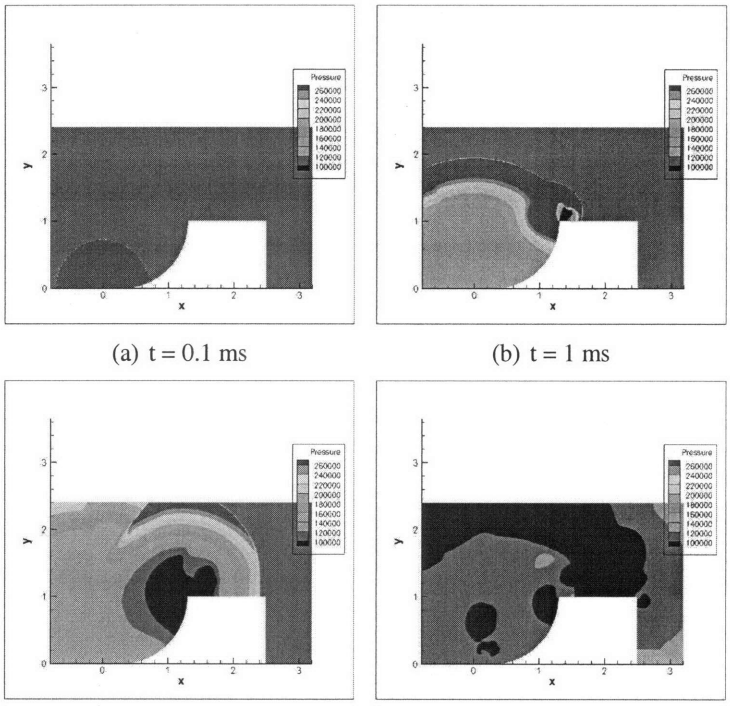

(a) t = 0.1 ms (b) t = 1 ms

(c) t= 3 ms (d) t = 7 ms

Figure 4-8: Snapshots of blast flow over a concave hull at different time instants

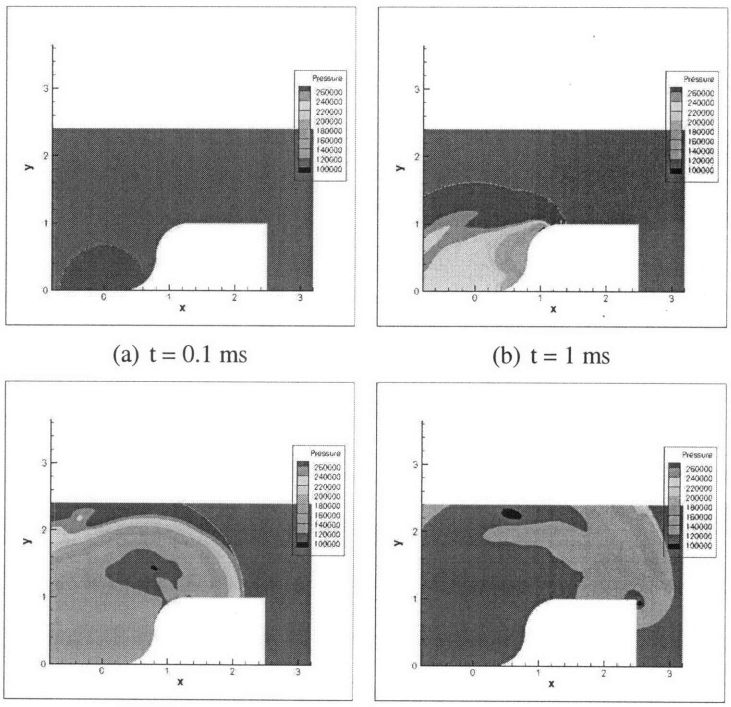

(a) t = 0.1 ms (b) t = 1 ms

(c) t= 3 ms (d) t = 7 ms

Figure 4-9: Snapshots of blast flow over a concave-convex hull at different time instants

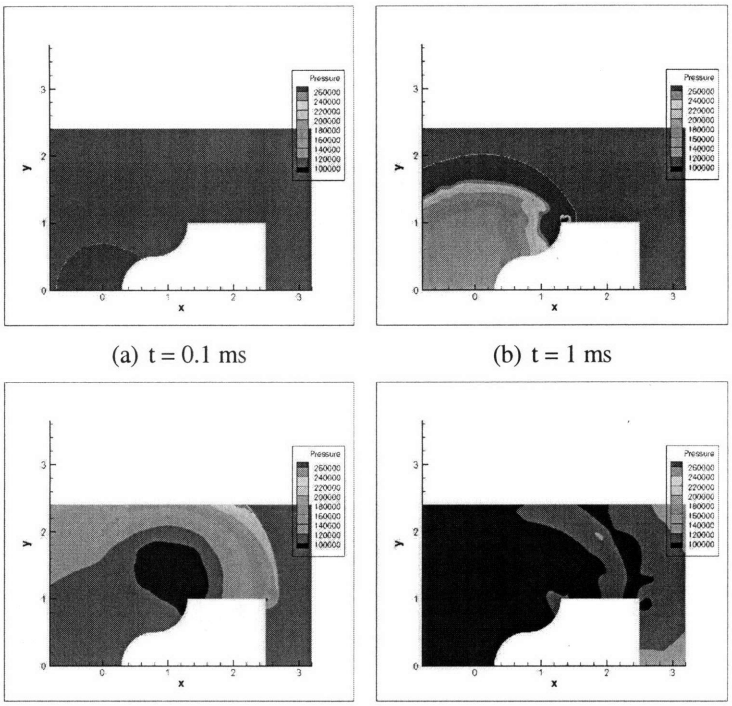

(a) t = 0.1 ms (b) t = 1 ms

(c) t= 3 ms (d) t = 7 ms

Figure 4-10: Snapshots of blast flow over a convex-concave hull at different time instants

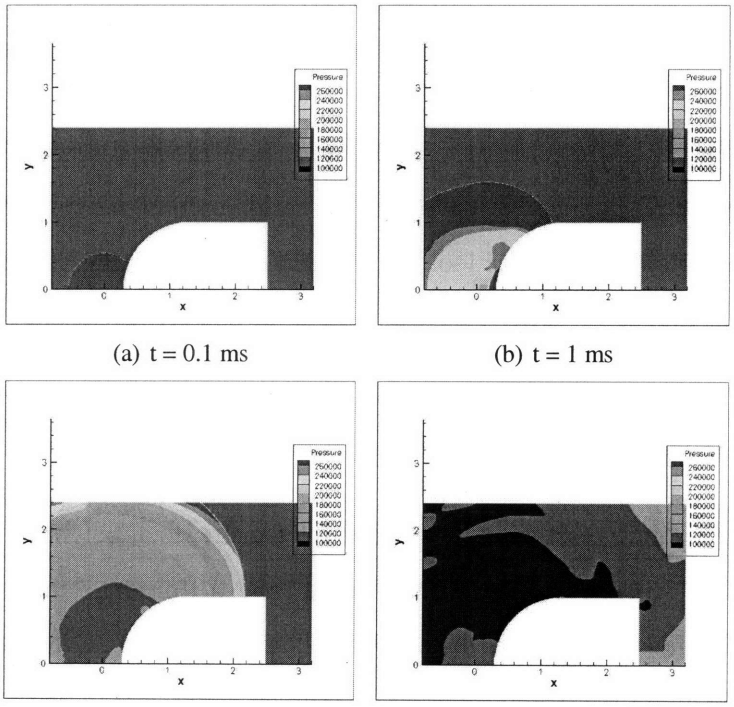

(a) t = 0.1 ms (b) t = 1 ms

(c) t= 3 ms (d) t = 7 ms

Figure 4-11: Snapshots of blast flow over a convex hull at different time instants

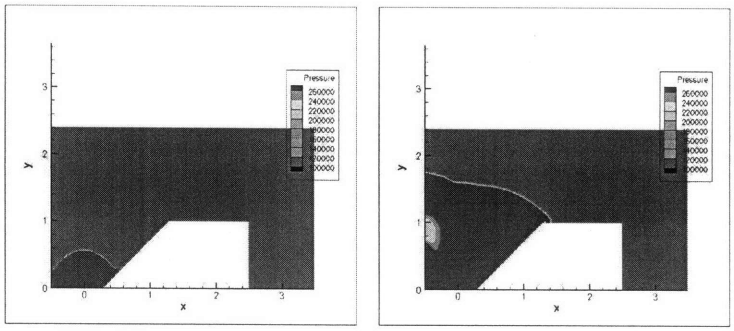

(a) t = 0.1 ms (b) t = 1 ms

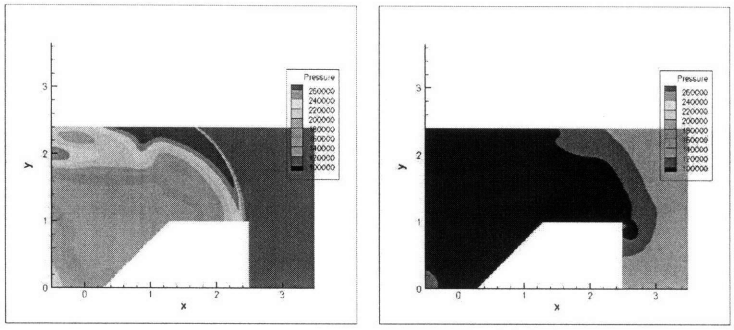

(c) t= 3 ms (d) t = 7 ms

Figure 4-12: Snapshots of blast flow over a V-shaped hull at different time instants

4.2 A more detailed look at V-shapes

From previous results for generic shapes, it can be seen that the V-shape offers the minimum value for peak head-on impulse, the primary criterion used in measuring the impact on the solid. In the following study we look at the effect of changing the SOD, keeping the floor height a constant.

4.2.1 Initial conditions

We consider a solid object with a half width of 1 metre, total height of 2.5 metres, and a floor height of 1.3 metres. The SOD is varied from 0.3 m to 1.3 m. It can be seen that when the floor height is same as the SOD, the shape is nothing but the flat-shape. As done earlier, the body is assumed to be rigid and stationary and doesn't deform or move during the course of the simulation.The point source solution is solved upto a distance of 2 cm lesser than the SOD and is provided as the initial condition of the blast wave.

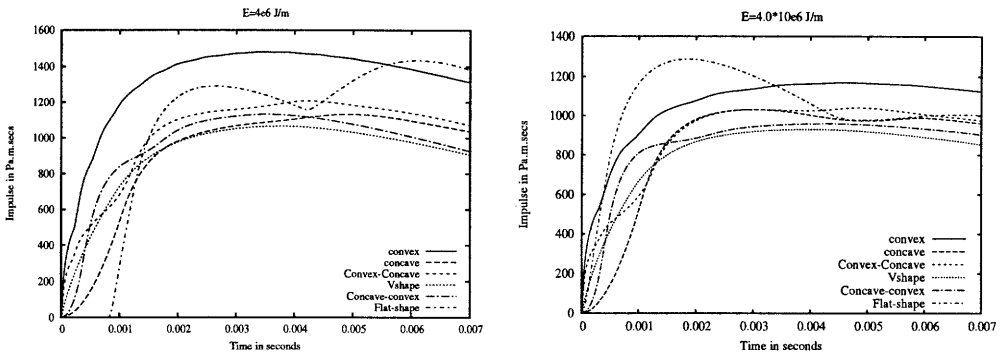

(a) Symmetry on left boundary

(b) Outflow on left boundary

Figure 4-13: Effect of changing boundary condition on the impulse evolution for various shapes

4.2.2 Boundary conditions

We assume the same boundary conditions as that for a surface blast. So reflection boundary conditions are applied at the left and bottom boundary while the other two boundaries have outflow conditions.

Simulations are run for a total time of 7 ms and the results from the simulation are presented below:

Shown in Figure 4-14 are the results of maximum head-on impulse versus SOD for 4 different blast intensities. From the plots it can be seen that as the SOD is increased, the impulse value drops to a minimum, remains nearly a constant over a range of SOD values, and then rapidly increases monotonically beyond this range. This range is relatively a constant over all the values of blast intensities and corresponds to around (0.4m , 0.7m) for the given configuration. The impulse recorded over this range varies between 0.70 to 0.80 times of the peak impulse recorded for the flat plate for a given blast intensity, with this ratio increasing as the blast intensity is increased.

This suggests that, for the given geometry, any choice of SOD lying between 0.4 m and 0.7 m, the maximum head-on impulse is likely to be the minimum. Given this information alone, it would be wiser to choose a design with SOD to be the lowest(0.4 m) as we would like the vehicle's ground clearance to be as low as possible.

Figure 4-15 gives the values of the side-on impulse for varying SOD. In this case,

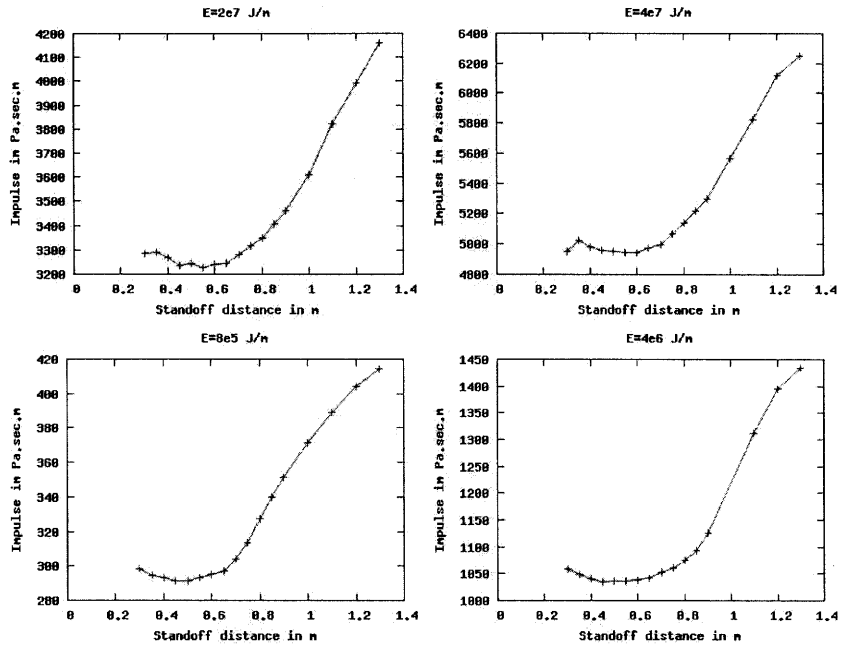

Figure 4-14: Maximum head-on impulse versus stand-off distance for V-plate

we notice that as SOD is increased, the side-on impulse value decreases. For the lowest energy level considered, i.e. blast intensity of 0.8 MJ/m, minimum impulse occurs for maximum SOD of 1.3 m which is equivalent to the no hull/flat plate case. As the blast intensity is increased, we noticed that the minimum impulse occurs for decreasing values of SOD, being 1.1 m for 4 MJ/m, 1.0 m for 20 MJ/m, and 0.9 m for 40 MJ/m of initial blast intensity respectively. The ratio of minimum to maximum value for the impulse for a given blast intensity is found to be nearly a constant around 0.65 for all blast intensities that were considered.

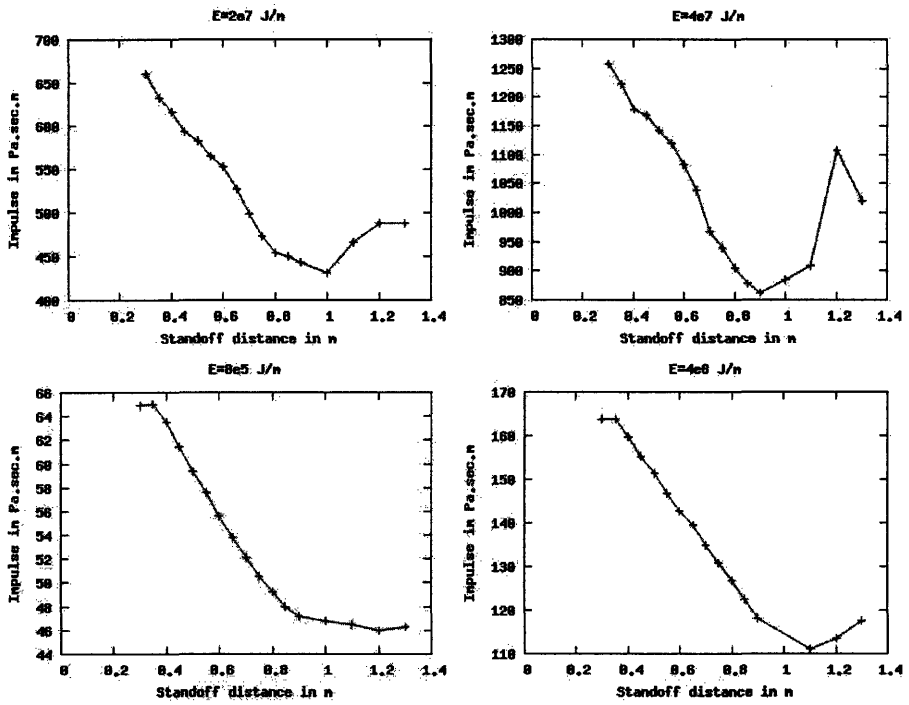

Figure 4-15: Maximum side-on impulse versus stand-off distance for V-plate

4.2.3 Changing the floor height

Our next step is to investigate the combined effects of changing the floor height and SOD on the maximum head-on impulse acting on the solid object. We assume the same initial conditions and boundary conditions as used earlier and keep the blast intensity fixed for each simulation at 4 MJ/m. A schematic shown in Figure 4-16 gives one an idea of what we refer to as the "floor height" and "Stand-off distance (SOD)".

Simulations are conducted for floor height values from 0.9 m to 1.3 m, in increments of 0.1 m. In each case, the range of SOD considered is from 0.3 m up to the floor height value for those corresponding set of simulations. It can be seen that we refer to the flat-shape/no hull case when the floor height and SOD are of the same value.

Figure 4-17 shows the influence of floor height and SOD on the peak head-on and side-on impulse values.

From Figure 4-17(a) it is obvious that decreasing the floor height leads to a jump in the peak head-on impulse values for a given SOD. This jump roughly corresponds to an

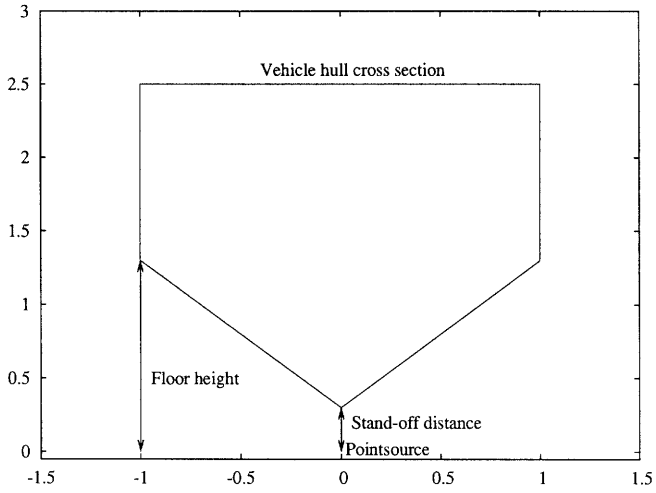

Figure 4-16: A schematic describing Stand-off distances(SOD) and floor heights

increase of 8-10 % in the peak impulse for a given SOD and for a decrease in floor height in 0.1 m and this percentage change increases slightly with decreasing floor height and increasing SOD. As seen earlier, for a given floor height, the peak impulse values are nearly constant over a range of low SOD values, and then show a steady monotonic increase when SOD increases beyond this range. The range of values over which the peak impulse values are nearly constant is variable with the floor height, and progressively decreases as the floor height is decreased.

Figure 4-18 shows the iso peak head-on impulse contours plotted with SOD and floor height along the X and Y axes. The impulse values have been plotted by approximating the peak impulse value to the nearest multiple of 50, and then plotting the iso-contours over the range of minimum value of 1050 Pa.m.sec to a maximum of 1700 Pa.m.sec with increments of 50. Bezier curve interpolation is used to connect the data points withthe same impulse value to obtain the corresponding contour curve.

This figure shows that the lowest impulse values are obtained when the SOD is minimized and floorheight is maximized. Another interesting fact to be noted is that there is a linear relationship between the SOD and floor height of the vehicle for a fixed peak impulse.

Peak side-on impulse values change with SOD and floor height as shown in Figure

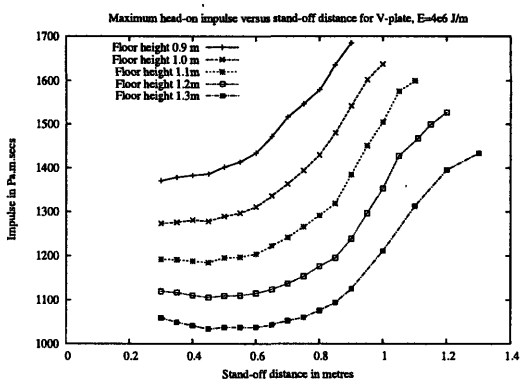

(a) Head-on impulse

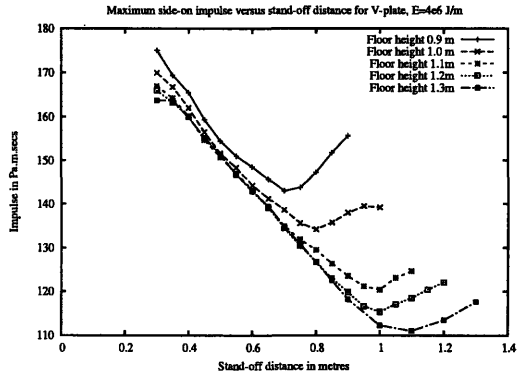

(b) Side-on impulse

Figure 4-17: Influence of floor height and SOD on the peak head-on and side-on impulse values in a V-shaped hull

4-17(b). The impulse values are nearly constant for lower SOD values, and the value is also constant for changing floor heights. However, unlike the head-on impulse values, the side-on impulse values decrease with increasing SOD. Also the magnitude of the impulse decreases as the floor height increases. Thus, in picking a design with minimum side-on impulse, we would prefer one with a higher SOD and floor height. In the set of simulations conducted, this minimum is observed for a floor height of 1.3 m and a SOD of 1.1 m.

From the above discussion, it becomes clear that a choice of maximum floor height would be suitable in reduction of impulse for a V-shaped hull design. The best choices for SOD would be a compromise between low values(suitable for lower peak head-on impulse) and higher values(more suitable for lower peak side-on impulse).

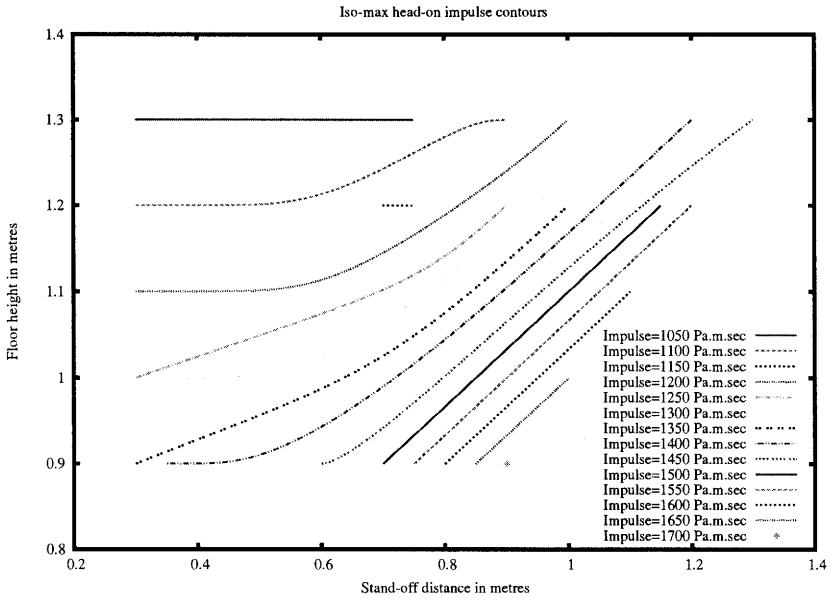

Figure 4-18: Iso-contours of peak head-on impulse for varying floor height and SOD

4.3 Changing V-shape

We observed that when the V-shapes are changed, there is a range of stand-off distances for which the maximum head-on impulse remains almost a constant minimum- being anywhere between 0.4 m and 0.7 m for the geometric considerations used in the earlier set of simulations. As a next step we explore the effect of changing the SOD continuously over time during the course of the simulation, and observe how it affects the head-on impulse acting on the body.

From the results it can be seen that positive velocities contribute towards an increase in head on impulse while negative velocities cause a decrease in the impulse. In other words, in going from shape shown in Figure 4-19(a) to Figure 4-19(b) there is an increase in head-on impulse as compared to a stationary case and vice-versa in going from Figure 4-19(b) to Figure 4-19(a). It is also seen that this increase/decrease in impulse value is proportional to the magnitude of front tip velocity. Thus the moving shape with velocity V= -300 m/s has the minimum head-on impulse while V=+300 m/sec has the maximum head-on impulse.

This might appear to be non intuitive as the results suggest that a shape which moves forward towards the blast actually has a lesser impact load on it as opposed to one which

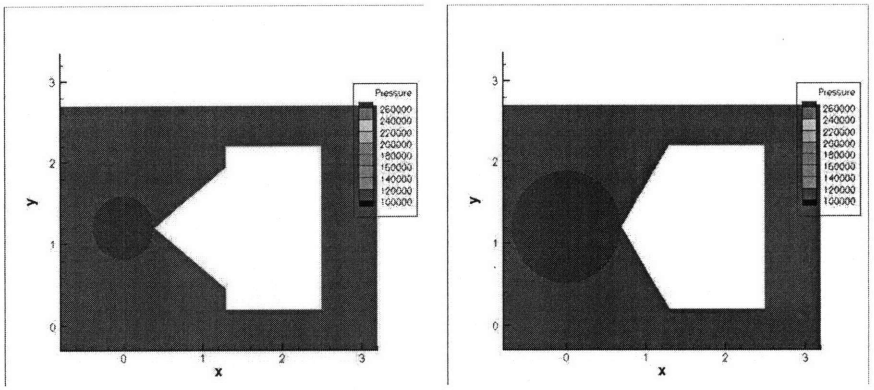

(a) Standoff = 0.4 m (b) Standoff = 0.7 m

Figure 4-19: Figure showing the two end configurations for the shapes with a movable hull

moves away from the blast. However it should be noted that in the this case, while the front tip moves forward towards the blast, the incident angle between the incoming blast wave and the vehicle hull increases. In the latter case it is vice versa.

It is possible that when the angle of incidence between the blast and hull plate increases, the reflected pressure as a ratio of the incident pressure decreases. This causes a drop in the net force acting on the object, as also the impulse obtained using Equation 4.3. Also, in this case, the initial SOD of the hull is 0.7 m, which is 0.3 m more than the other end configuration. In a cylindrical blast, the pressure is expected to vary roughly as $\frac{1}{R^2}$ where R is the radial distance from the point source. Hence the incident pressure at an SOD of 0.7 m would be nearly 3 times lesser than the incident pressure at an SOD of 0.4 m.

The percentage reduction of impulse at V = -300 m/s over the stationary cases is around 20 %. This means it could be a good means of active mitigation against blast impact. We already know from our previous analyses that the V-shaped hull is capable of providing maximum protection against head-on impulse amongst all generic shapes. In this study we have compared the results for the moving plates with the best performing stationary shapes amongst all V-plates, and we are able to show that it is possible to further reduce the impulse by 20 % if we choose flexible designs with an active blast mitigation capability.

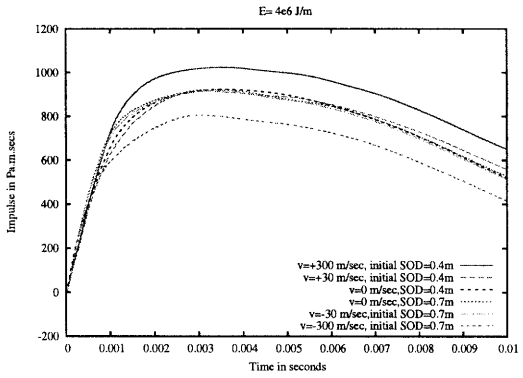

(a) Head-on impulse evolution curves

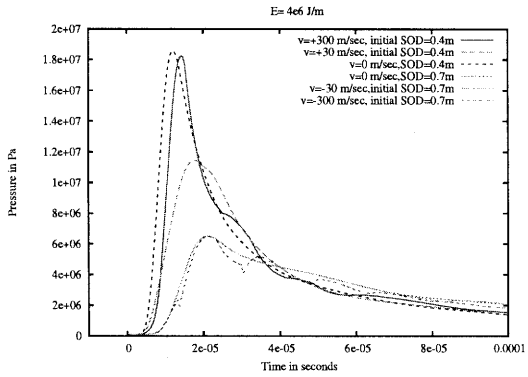

(b) Evolution of pressure at the front tip

Figure 4-20: Figure showing the Impulse evolution and Pressure evolution at the front tip of the moving plates over time

4.4 Optimization of shape

Earlier analyzes that were conducted in our research study have dealt with a range of shapes defined by a set of parameters that take discrete values. For example in our study of V-shapes, we defined the SOD and the floor height as our variable parameters which can take discrete values, and we do a sweep over allowable ranges of these parameters and determine the minimum value of the peak impulse.

Another approach to determine the values of these best set of parameters would be to set up an optimization problem where we define an objective function that needs to be minimized/maximized, the variable parameters, and constraints on the variables defined. In setting up such an optimization problem for our study, we define the peak head-on impulse acting on the solid as our objective function, geometrical parameters depending on the

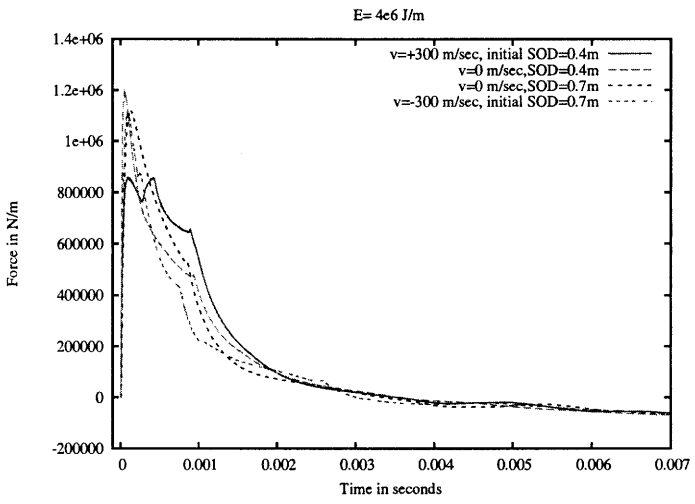

Figure 4-21: Head-on force evolution for moving plates

class of shapes considered as our variables, and constraints depending on the geometrical requirements from the problem under focus.

For these type of problems, an analytical function mapping the variable parameters to the objective function does not exist. Such type of problems are typically solved either by using iterative methods or using genetic algorithms(GA). For our study, iterative methods are more suitable than genetic algorithms. This is so because genetic algorithms usually need evaluation of the objective function over a large number of trial points before convergence is guaranteed. Every single evaluation in our study involves running the code to completion and then determining the maximum impulse. This requires a lot of computational effort and time and hence GA would not be suitable to our problem. Hence we proceed with the use of a numerical scheme based on iterative methods.

4.4.1 Optimization scheme

We set up the problem to be solved using the gradient projection algorithm, which is the natural extension of the steepest descent method to bound constrained problems. The solution scheme for this method is obtained from [39].

Given current iterate x_k, the new iterate is

$$x_{k+1} = \mathcal{P}(x_k - \lambda \nabla f(x_k)) \tag{4.4}$$

where λ is a steplength parameter given by the simple Armijo line search rule and $\mathcal{P}$ is a projection operator given as

$$\mathcal{P}(x)_i = \begin{cases} L_i & if (x)_i \leq L_i, \\ (x)_i & if L_i < (x)_i < U_i, \\ U_i & if (x)_i \geq U_i. \end{cases} \tag{4.5}$$

where L_i and U_i are the lower and uppper bounds for the variable x.In order to implement any line search scheme, we must specify what we mean by a sufficient decrease. For $\lambda > 0$ define

$$x(\lambda) = \mathcal{P}(x - \lambda \nabla f(x)) \tag{4.6}$$

For bound constrained problems sufficient decrease conditions for line searches are expressed as

$$f(x(\lambda)) - f(x) \leq \frac{-\alpha}{\lambda} ||x - x(\lambda)||^2 \tag{4.7}$$

where α is a paramater that one typically sets to 10^{-4} [40].Following gives a description of the numerical algorithm used.

1. *For* $n = 1, \ldots, nmax$

   (a) Compute f and ∇f; test for termination.

   (b) Find the least integer m such that Equation 4.7 holds for $\lambda = \beta^m$.

   (c) $x = x(\lambda)$.

2. If n = nmax and the termination test is failed, signal failure.

It must also be noted that for a constrained optimization problem, ∇f need not be zero at the solution. A natural substitute used is to terminate the iteration if the difference between x and x(1) is small. A test study is conducted for a single variable parameter and details for this test are presented below.

4.4.2 Test study with Elliptical shapes

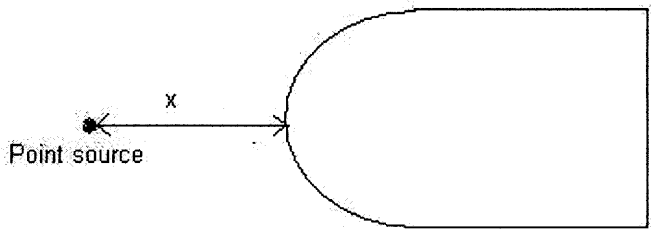

Figure 4-22: Schematic of the elliptic hull shape used for the optimization study

Shown in Figure 4-22 is the schematic layout for the geometry used in our study. We consider the set of semi-elliptical shapes for the hull with one axis of the ellipse being fixed and the other axis being variable in length. The SOD measured as the distance from the point source to its closest point on the hull is used as the variable paramater x in this simulation. The width and length of the box behind the hull on the solid are kept constant at 0.4 m. Initial conditions included the initialization of the point blast code up to a distance of 0.02 m lesser than the SOD. Input parameters supplied to the blast code include

$$\begin{aligned} \text{Ambient pressure } p_0 &= 101214Pa \\ \text{Ambient density } \rho_0 &= 1.22\frac{kg}{m^3} \\ \text{Blast intensity } E_0 &= 4 \times 10^6 Joules \\ \gamma &= 1.4 \end{aligned} \tag{4.8}$$

Boundary conditions include outflow on all the boundaries, and the solid is kept rigid and fixed. The peak head-on impulse measured from these simulations is used as the objective function and results from the optimization study are given in Table 4.1

From this study we observed that our objective function is minimized for x=0.58878 m, and the minimum value for the objective function is 165.27 Pa.m.s. The study took overall 18

Iteration number	Number of sub-steps	x(in m)	Function value at end of iteration(In Pa.m.s)
1	1	0.40000	190.99
2	1	0.72095	174.57
3	4	0.57638	168.55
4	5	0.59040	165.38
5	7	0.58878	165.27

Table 4.1: Results from an optimization study on elliptic shapes

runs(including all the sub-iterations) of the simulation to obtain the optimized shape. The results are compared with a discrete numerical study whose results are shown in Figure 4-23. Simulations are run for SOD varying from 0.3 m to 0.9 m with increments of 0.05 m. Once the shape corresponding to the lowest value of the peak impulse is identified among these, a local refinement to 0.01 m is used. As observed from the figure below, a tip distance of 0.59m gave the minimum value for the objective function and this result compares well with the optimization study.

Although, the optimization study is extremely fast, it may or may not always converge. This is so because the objective function f is obtained by running a simulation in a fluid grid which is prone to numerical errors arising for the "staircase" artifacts along the internal boundaries. Hence f is not necessarily a smoothly varying function, and local fluctuations in the function value around a data point can lead to inaccurate results in an iterative scheme which is dependent on the gradient of the function for convergence. On the other hand, the discrete numerical sweep study requires a comparable amount of computational effort as the optimization scheme, but is relatively more straight forward and gives more reliable results.

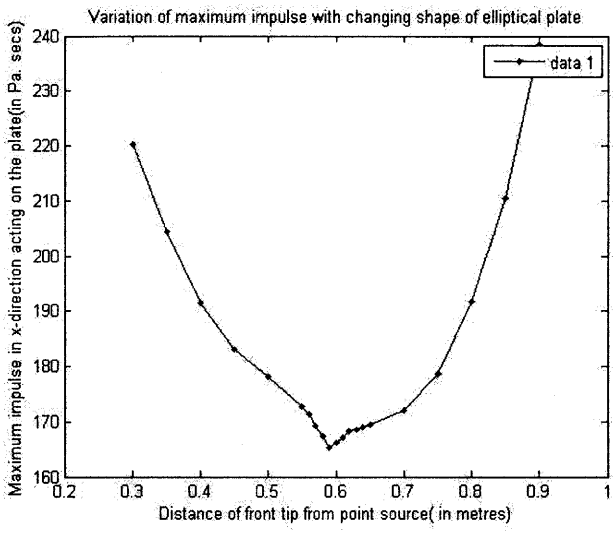

Figure 4-23: Discrete numerical study for semi-elliptical hull shapes

4.5 Three dimensional simulations

Following from the earlier studies, we conduct simulations of blast-vehicle interaction in a 3 dimensional environment. The mechanics of the fluid-structure interaction have been described in Section 3.2. From our earlier results for 2D, we were able to observe that the V-shaped hull is the most effective among all the generic shapes considered in minimizing the peak head-on impulse values. In the following study we compare a 3D model of a V-shaped hull with another model which does not possess a hull. The details of these set of simulations are presented below.

4.5.1 Geometry

Two particular solid models are considered :

- **Flat-box**: This corresponds to a hollow rectangular box with the outer dimensions: $0.4m \times 0.4m \times 0.4m$. The thickness of the box is taken to be 2 cm.

- **V-shaped box**: This corresponds to an object with the same dimensions as that of a flat-box, but also having a V-shaped hollow hull attached to one of its faces. The height of the hull is 0.3 metres and it has a thickness of 2 cm.

Shown in Figure 4-24 are the meshes for the two types of solid that are quoted above. These shapes are a scaled down representation of an actual vehicle, with the flat box representing the passenger compartment, and the V-shaped hull being the blast deflector attached to the bottom face of the vehicle. Scaled down models are used in this study to reduce computational costs associated with 3D simulations.

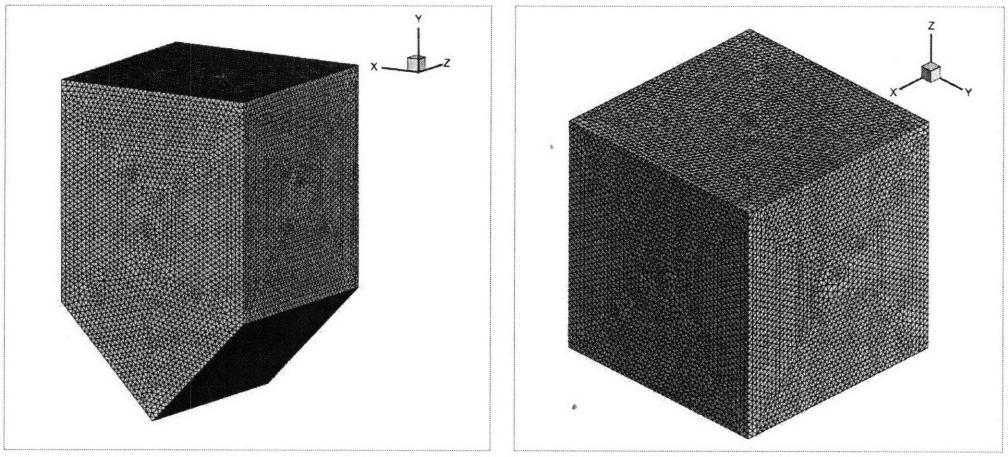

(a) Mesh for the V-shaped box (b) Mesh for the flat-box

Figure 4-24: Figure showing the meshes for the two types of solid considered in the 3D simulations

4.5.2 Initial conditions

The point source blast solution described in Chapter 2 is solved and interpolated over the 3D fluid grid to initialize a spherical blast wave. The input parameters supplied to the blast code are

$$\begin{aligned} \text{Ambient pressure } p_0 &= 101214Pa \\ \text{Ambient density } \rho_0 &= 1.22\frac{kg}{m^3} \\ \text{Blast intensity } E_0 &= 4 \times 10^6 Joules \\ \gamma &= 1.4 \end{aligned} \tag{4.9}$$

The point source origin is set to be 0.7 m below the the center point on the floor of the vehicle in both cases. Thus SOD for the Flat-box is thus 0.7 m and for the V-shaped box it

Table 4.2: Material model parameters for stainless steel.

Mass density ρ [kg·m^{-3}]	Young modulus E [GPa]	Poisson ratio ν	σ_0^y [MPa]	η_ε	ε_0	$\eta_{\dot{\varepsilon}}$	$\dot{\varepsilon}_0$ [s^{-1}]
7880	190	0.3	365	1.19	0.136	4.82	14518

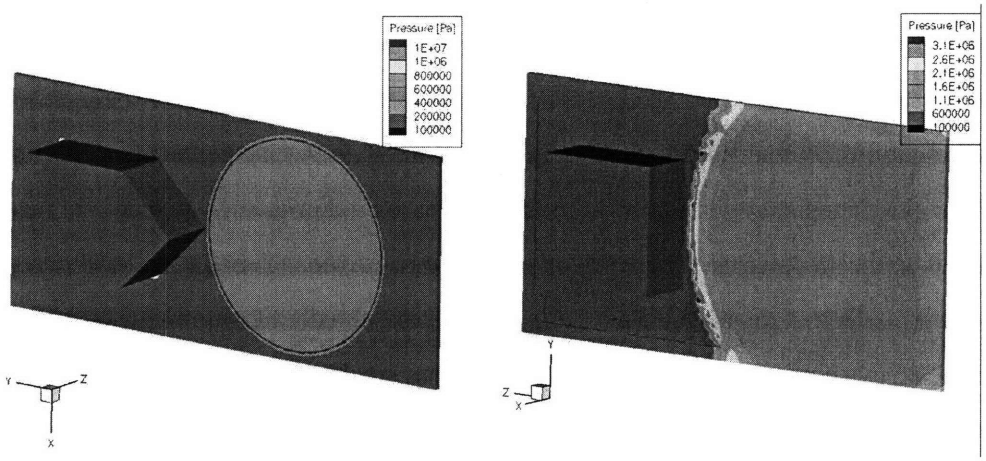

(a) Fluid solid representation for the V-shaped hull (b) Fluid solid representation for the no hull body body

Figure 4-25: Figure showing the FSI simulations conducted in VTF using 3D models

is 0.4 m. In either case, the point source is initialized up to a distance of 2 cm lesser than the SOD. Figures 4-25(a) and 4-25(b) show the initial conditions of the 3D fluid-structured interaction problem that we consider in our studies.

The solid is modeled as stainless steel whose elasto-plastic response was modeled with an isotropic model of large-deformation plasticity. The hardening and rate-dependence of the instantaneous yield stress is given by the power-law:

$$\sigma^y = \sigma_0^y \left[1 + \left(\frac{\varepsilon^{\text{pl}}}{\varepsilon_0} \right)^{\frac{1}{\eta_\varepsilon}} + \left(\frac{\dot{\varepsilon}^{\text{pl}}}{\dot{\varepsilon}_0} \right)^{\frac{1}{\eta_{\dot{\varepsilon}}}} \right] \tag{4.10}$$

where σ^y is the effective flow stress, σ_0^y is the initial von Mises yield stress, η_ε is the strain hardening exponent, ε^{pl} is the equivalent plastic strain, ε_0 is the reference plastic strain, $\eta_{\dot{\varepsilon}}$ is the strain rate exponent, $\dot{\varepsilon}^{\text{pl}}$ is the plastic strain rate and $\dot{\varepsilon}_0$ is the reference plastic strain rate. The values for stainless steel are given in table 4.2.

4.5.3 Boundary conditions

Outflow conditions are assumed on all the six faces of the fluid grid. Also, no boundary conditions are applied on the solid mesh, implying that it is a free standing object. The size of the fluid grid used in these set of simulations is $0.8m \times 0.8m \times 1.6m$.

4.5.4 Simulation setup

Simulations are run for a total time of up to 2 ms with outputs taken every 50 time steps. The mesh consists of $40 \times 40 \times 80$ cells on the base fluid grid, and 3 levels of refinement are used on the Adaptive mesh framework generated by AMROC. Each sub level of refinement corresponds to a decrease in mesh size by 0.5. Nominal CFL number used for each fluid time step is controlled to be close to 0.9, and any given time step is repeated with a restart from the earlier step if the CFL number exceeds over 0.99.

The solid meshes for each shape are created using tetrahedral elements with a seed size of 0.02 m in ABAQUS. In the case of flat-box, this mesh contains 19747 elements with a minimum shape factor of 0.16, while the meshes for the V-shaped box consist of 21768 elements with a minimum shape factor of 0.21.

Simulations are run on 8 processors using 5 processors for the fluid solver and the rest for the solid solver. Fluid-structure coupling is enabled between the two solvers as described in Section 3.2.3. From the output files obtained from the solid solvers at every fiftieth time step, we determine the pressure acting on all the nodal points of the solid at that time step. Using this information, we can compute the total force acting on the solid and integrate it over time to obtain the impulse acting on the solid over time.

4.5.5 Results and analysis

Shown in Figure 4-26 are the results for the different impulse evolution curves obtained by integrating the force acting on the different faces of the solid objects. Figure 4-26 (a) gives a comparison of the impulse evolution on the front face/hull of the V-shaped box and flat-box. This is a measure of the direct impact from the blast wave beneath the vehicle body on the vehicle. It can be seen that at t = 1.3 ms, the impulse for the V-shaped box

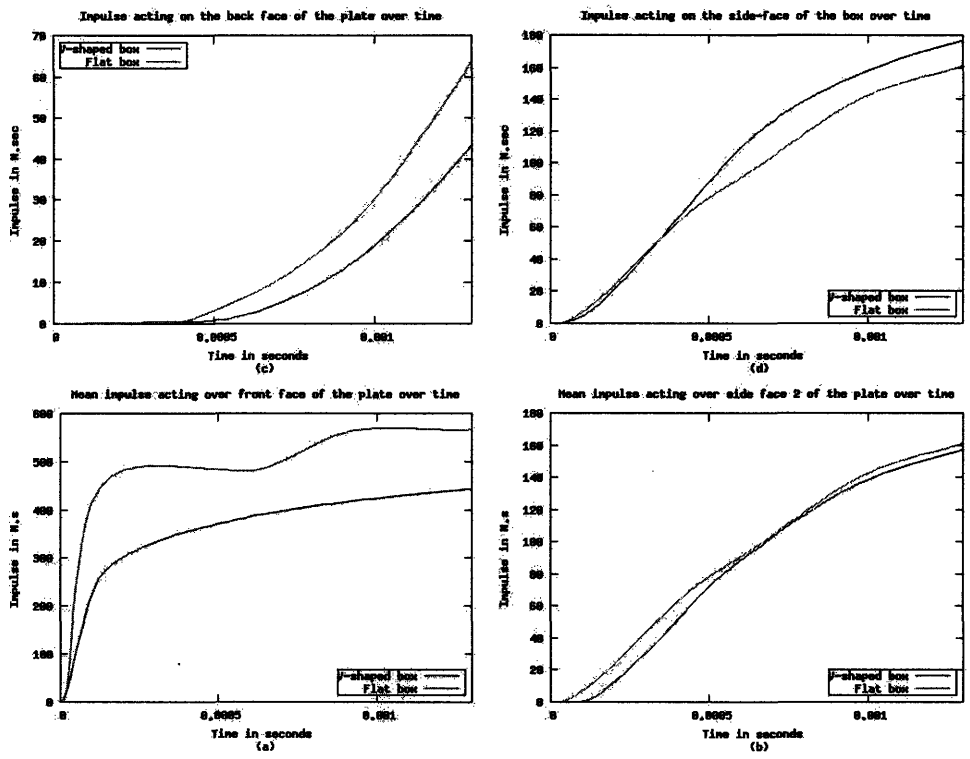

Figure 4-26: Comparison of different impulse evolutions between the flat-box and the V-plate box

is 420 N.s while it is close to 580 N.s for the flat-box. Therefore the V-shaped hull leads to a 30% reduction in the impulse as compared to a flat-bottomed vehicle. Figure 4-26(b) and Figure 4-26(d) show the impulse evolution on the 2 side faces of the solid object owing to the impact from the blast. It is seen there that is less than a 10% difference between the V-shaped box and the flat-box for the side-on peak impulse at t = 1.3 ms. Figure 4-26 (c) shows the impulse evolution curves for the back faces of the two boxes, which would correspond to the top face of a vehicle. Although we notice some difference in the impulse evolution curves for the two cases considered, the effect on the net impulse acting on the vehicle will be negligible as the magnitude of these impulse values are very low.

Figure 4-27 gives the specific impulse and pressure evolution at the center point of the hull in the two cases considered. Specific impulse at a given point is obtained by integrating the pressure acting on that point over time. Comparing the two sets of curves, we see that the specific impulse for the flat-box is higher even though the peak pressure is higher for

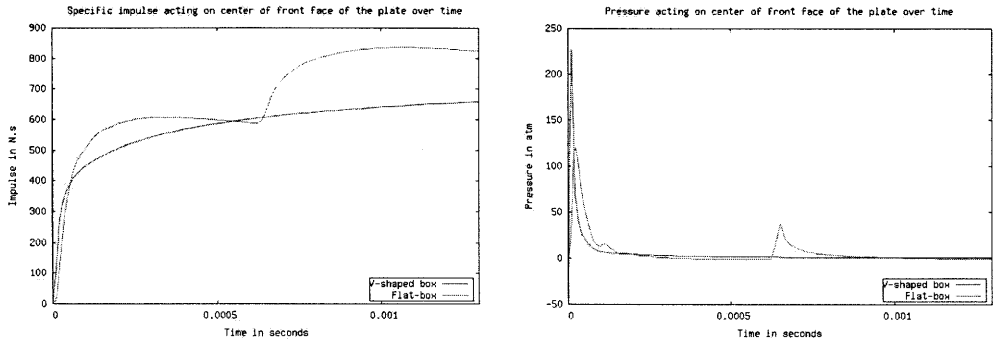

(a) Specific impulse at the center of the front face (b) Pressure at the center of the front face

Figure 4-27: Figure showing the pressure and Specific impulse evolution at the center of the front face of the two objects considered

the V-shaped box. The reason for this is that the secondary reflected shock waves which affect the flat-box and are not observed in the case of the V-shaped box. Due to these secondary reflected shocks, we observe multiple peaks on the pressure evolution curve for the flat-box and this also the causes the multiple humps on the mean impulse and specific impulse curves. This shows us the advantage of using V-shaped hulls because they deflect the incoming blast wave and do not suffer from secondary reflected shock loadings unlike the flat-bottomed hulls.

Chapter 5

Conclusions

We have conducted analyses of the blast wave-vehicle body interaction in both two dimensional and three dimensional environments. A wide range of shapes and blast intensities were considered and the impact of the blast on the vehicle body was measured in terms of the head-on impulse and side-on impulse acting on the body. Based on our observations, we can say that the V-shape showed the best performance amongst all the shapes considered in reducing the peak head-on impulse. Shapes with a small angle of incidence to the incoming blast wave (such as convex and other flat shapes) were affected by the secondary reflected blast wave leading to peak head-on impulse values which were as much as 40 % more than V-shapes under similar conditions. This result was also confirmed with 3D simulations where it was shown that V-shapes show over a 20 % reduction in the peak head-on impulse when compared to flat-shaped hulls.

On the other hand, concave and convex-concave shapes showed a significant reduction in the impulse acting on the sides of the vehicle. Peak head-on impulse values were 7 times or more higher than the corresponding peak side-on impulse values for low blast intensities(E=4e6 J/m), but this ratio reduced significantly in magnitude when higher blast intensities were considered. This leads to the conclusion that side-on impulse values may have to be considered in the design of hull shapes for protection against blasts of much higher intensities.

As the next step, a deeper analysis of V-shapes was conducted by considering the effect of changing floor height and SOD on the blast impact on the vehicle. It was seen that

head-on impulse values were nearly constant and minimum for a range of SOD values. Beyond this range, the peak head-on impulse showed a steady rise until the SOD was equal to the floor height, in which case it corresponds to a flat-shape. Decrease in floor height, i.e. lowering the vehicle floor, showed a drastic increase in the peak head-on impulse. Therefore the best choice of shapes for the V-shaped hull were those with the maximum floor height and a SOD which had to be picked from a range of values for minimum peak head-on impulse. This value was chosen by considering the peak side-on impulse values over this range of SODs. It was seen that for a given floor height, when the SOD value was increased, it resulted in a decrease in peak side-on impulse. Using this information, we pick the value of SOD to be the maximum from the range of values available so that both peak head-on impulse and peak side-on impulse were minimized. For the geometries considered in our study(which roughly corresponds to the cross-section of a Cougar H MRAP vehicle), the best choice of value for the SOD is 0.8 m and the best choice for the floor height is 1.3 m.

The future direction of work from this study would be towards a complete analysis of these shapes under realistic loading conditins. In doing so, we will need to develop soil models, and also a good understanding of the blast wave-soil-structure interaction. These blast loading models must then be used with accurate three dimensional models of the MRAP vehicle and thereafter impact measurements must be made.

Bibliography

[1] The Washington Post. Navistar maxxpro.

[2] Force Protection Inc. Cougar h mrap vehicle.

[3] Ideal Innovations. Ceradyne bull.

[4] D. Bogosian, J. Ferritto, and Y. Shi. Measuring uncertainty and conservatism in simplified blast models. *Presented at the 30th Explosives Safety Seminar, Atlanta, Georgia*, August 2002.

[5] Washington Post. More attacks, mounting casualties.

[6] USA today. Us military struggles to adapt to war's top killer.

[7] The Weekly Standard. Bae's rg-31 nyala mine protected vehicle.

[8] USA today. The truck the pentagon wants and the firm that makes it.

[9] K Genson. Vehicle shaping for mine blast damage reduction. Master's thesis, University of Maryland, College Park, 2006.

[10] A.D. Gupta and R.R. Skaggs. Effect of deflector shapes on mine-blast loading. Technical Report ARL-TR-3042, Army Research laboratory, 2003.

[11] J.E. Tremblay. Impulse on blast deflectors from a landmine explosion. Technical Report DREV-TM-9814, Defense research establishment, Quebec, 1998.

[12] P.S. Westin, B.L. Morris, P.A. Cox, and E.Z. Polch. Development of computer program for floor plate response from land mine explosions. Technical Report Technical Report No. 13045, US Army Tank-Automotive Command, 1985.

[13] G. Fairlie and D. Bergeron. Numerical simulation of mine blast loading on structures. *17th Military aspects of blast symposium*, 2002.

[14] D. Fiserova. Validation of a loading model for simulating blast mine effects on armoured vehicles. *PhD Thesis: Cranfield University*, 2006.

[15] H.L. Brode. Numerical solution of spherical blast waves. *Journal of Applied Physics*, 26(6):766–775, 1955.

[16] G.I. Taylor. The formation of a blast wave by a very intense explosion, I theorical discussion. *Proceeding of Royal Society, Series A*, 201(1065):159–174, 1950.

[17] J.D. Anderson. *Fundamentals of Aerodynamics*. McGraw-Hill, 2001.

[18] PD Smith and JG Hetherigton. *Blast and ballistic loading of structures*. Butterworth Heinemann, 1994.

[19] J. Von Neumann. The point source solution. In A. J. Taub, editor, *John von Neumann: Collected Works*, volume 6, pages 219–237. Permagon Press, 1963.

[20] N. Kambouchev. Analysis of blast mitigation strategies exploit fluid-structure interaction. *PhD Thesis: Massachusetts Institute of Technology*, 2007.

[21] L. I. Sedov. *Similarity and Dimensional Methods in Mechanics*. CRC Press Inc., Florida, 1993.

[22] H.H. Goldstine and J. Von Neumann. Blast wave calculation. *Communications in Pure and Applied Mathematics*, 8:327–354, 1955.

[23] D.E. Okhotsimskii, I.A. Kondrasheva, Z.P. Vlasova, and R.K. Kozakova. Calculation of a point explosion taking into account counter pressure. *Tr. Mat. Inst. Steklova*, 50:1–65, 1957.

[24] T. Bui-Thanh. Calculation of a point explosion taking into account counter pressure. Technical report, Department of Aeronautics and Astronautics, MIT, 2007.

[25] J.K. Clutter, J.T Mathis, and M.W. Stahl. Modeling environmental effects in the simulation of explosion events. *International Journal of Impact Engineering*, 34:973–989, 2007.

[26] T. Bui-Thanh. Point source solution validation. Technical report, Department of Aeronautics and Astronautics, MIT, 2007.

[27] R. Deiterding. A generic framework for blockstructured adaptive mesh refinement in object-oriented C++. http://amroc.sourceforge.net/.

[28] R.J. Leveque. Conservative Laws software Package. http://www.amath.washington.edu/ rjl/clawpack.html.

[29] S. Osher and R. Fedkiw. *Level set methods and dynamic implicit surfaces*. Springer, New York, 2003.

[30] R.P. Fedkiw, T. Aslam, B. Merriman., and S. Osher. A non-oscillatory Eulerian approach to interfaces in multimaterial flows(the ghost fluid method). *jcp*, 152:457–492, 1950.

[31] R. Deiterding, R. Radovitzky, S.P. Mauch, L. Noels, J.C. Cummings, and D.I. Meiron. A virtual test facility for the efficient simulation of solid material response under strong shock and detonation wave loading. *Engineering with computers*, 22:325–347, 2006.

[32] Dassault systems. Simulia(formerly known as Abaqus). http://simulia.com/.

[33] The Virtual Test Facility. http://wiki.cacr.caltech.edu/asc/bin/view/VTFOverview/WebHome.

[34] J.E. Marsden and T.J.R. Hughes. *Mathematical foundations of elasticity*. Dover Publications, 1993.

[35] S.P. Mauch. *Efficient algorithms for solving static Hamilton-Jacobi equations*. PhD thesis, California Institute of Technology, 2003.

[36] F. Cirak and R. Radovitzky. A lagrangian-eulerian shell-fluid coupling algorithm based on level sets. *Computers and Structures*, 83:491–498, 2005.

[37] D. Tam, R. Samtaney, and R. Radovitzky. An algorithm for modeling the interaction of a flexible rod with a two-dimensional high-speed flow. *International Journal for Numerical Methods in Engineering*, 64:1057–1077, 2005.

[38] J. Cummings, M. Aivazis, R. Samtaney, R. Radovitzky, S. Mauch, and D. Meiron. A virtual test facility for the simulation of dynamic response in materials. *Journal of Supercomputing*, 23:39–50, 2002.

[39] T.C Kelly. *Iterative Methods for Optimization*. SIAM.

[40] *Numerical methods for unconstrained optimization and Nonlinear equations*. SIAM, 1996.

[41] L. Noels. Modelization of blast-body interaction. Technical report, Massachusetts Institute of Technology, 2006.

[42] C. N. Kingery and G. Bulmash. Airblast parameters from TNT spherical air burst and hemispherical surface burst. Technical Report ARBRL-TR-02555, Ballistic Research Laboratory, Aberdeen Proving Ground MD, 1984.